nature immunology

ARTICLES

https://doi.org/10.1038/s41590-019-0526-7

Identification of a novel arthritis-associated osteoclast precursor macrophage regulated by FoxM1

Tetsuo Hasegawa[1,2], Junichi Kikuta[1,3], Takao Sudo[1], Yoshinobu Matsuura[1], Takahiro Matsui[1], Szandor Simmons[1], Kosuke Ebina[4], Makoto Hirao[4], Daisuke Okuzaki[5], Yuichi Yoshida[6], Atsushi Hirao[7], Vladimir V. Kalinichenko[8], Kunihiro Yamaoka[2], Tsutomu Takeuchi[2] and Masaru Ishii[1,3]*

Osteoclasts have a unique bone-destroying capacity, playing key roles in steady-state bone remodeling and arthritic bone erosion. Whether the osteoclasts in these different tissue settings arise from the same precursor states of monocytoid cells is presently unknown. Here, we show that osteoclasts in pannus originate exclusively from circulating bone marrow-derived cells and not from locally resident macrophages. We identify murine $CX_3CR1^{hi}Ly6C^{int}F4/80^+I\text{-}A^+/I\text{-}E^+$ macrophages (termed here arthritis-associated osteoclastogenic macrophages (AtoMs)) as the osteoclast precursor-containing population in the inflamed synovium, comprising a subset distinct from conventional osteoclast precursors in homeostatic bone remodeling. Tamoxifen-inducible *Foxm1* deletion suppressed the capacity of AtoMs to differentiate into osteoclasts in vitro and in vivo. Furthermore, synovial samples from human patients with rheumatoid arthritis contained $CX_3CR1^+HLA\text{-}DR^{hi}CD11c^+CD80^-CD86^+$ cells that corresponded to mouse AtoMs, and human osteoclastogenesis was inhibited by the FoxM1 inhibitor thiostrepton, constituting a potential target for rheumatoid arthritis treatment.

Macrophages comprise a variety of subsets with diverse biological activities, contributing to tissue homeostasis and a broad spectrum of pathogenesis[1–4]. In response to environmental cues, they follow distinct developmental pathways, such as differentiation into osteoclasts. Osteoclasts are myeloid lineage cells with unique bone-destroying capacity, and require macrophage-colony stimulating factor (M-CSF) and receptor activator of nuclear factor κB ligand (RANKL) for differentiation and survival[5,6]. They play a key role in maintaining skeletal homeostasis by supporting steady-state bone remodeling in the bone marrow (BM). However, in contrast with this physiological role, osteoclasts are also involved in pathological arthritic bone erosion in patients with rheumatoid arthritis, which occurs where the hypertrophied synovium[7] (called 'pannus') invades the outer surface of the articular bone[6]. Previous studies have determined that the $Ly6C^{hi}$ monocytic population in the BM contains osteoclast precursors in arthritic mice[8,9], and have demonstrated that CX_3CR1 could be a marker for osteoclasts differentiated from BM-derived dendritic cells[10]. Nevertheless, a precise analysis of osteoclast precursors has not yet been performed in inflamed synovium—the actual site of bone erosion in arthritis—mainly due to technical difficulties associated with approaching and isolating tiny synovial tissues on the so-called 'bare area'[11], where bone is exposed to synovium without a cartilage covering, and is therefore vulnerable to erosion. It remains unknown whether these osteoclasts in the BM and synovial tissue settings share similar differentiation pathways and arise from similar precursor states of monocytoid cells[12]. In addition, while it has been suggested that osteoclasts in pannus derive from blood, the empirical evidence for this relationship is lacking.

In this study, we developed an original protocol to isolate the inflamed synovium on the bare area[11] of arthritic mice and identified $CX_3CR1^{hi}Ly6C^{int}F4/80^+I\text{-}A^+/I\text{-}E^+$ macrophages, which we termed arthritis-associated osteoclastogenic macrophages (AtoMs), as the osteoclast precursor-containing population in the arthritic joints, comprising a subset distinct from the BM osteoclast precursor-containing population[8,9,13]. We conducted a detailed assessment of the differentiation trajectory of arthritic osteoclast precursors, and FoxM1 inhibition suppressed the capacity of both mouse AtoMs and human $CX_3CR1^+HLA\text{-}DR^{hi}CD11c^+CD86^+$ cells to differentiate into osteoclasts. Collectively, these results show that AtoMs are the osteoclast precursor-containing population in the pannus tissue, and that FoxM1 constitutes a potential target for rheumatoid arthritis treatment.

Results

BM-derived CX_3CR1^+ cells differentiate into osteoclasts in inflamed synovium. To investigate the osteoclast precursor population in the inflamed synovium, we used a well-established experimental model—collagen-induced arthritis (CIA)—in DBA/1J mice. We developed an original protocol to expose the inflamed synovium on the bare area[11] of the femur by removing the patella, patellar ligaments and quadriceps femoris muscles together under a stereoscopic microscope, and isolating the tissue using microscissors (Supplementary Fig. 1a,b). After removal of the Achilles tendon, isolation of the

[1]Department of Immunology and Cell Biology, Graduate School of Medicine and Frontier Biosciences, Osaka University, Osaka, Japan. [2]Division of Rheumatology, Department of Internal Medicine, Keio University School of Medicine, Tokyo, Japan. [3]WPI Immunology Frontier Research Center, Osaka University, Osaka, Japan. [4]Department of Orthopaedic Surgery, Osaka University, Osaka, Japan. [5]Genome Information Research Center, Research Institute for Microbial Diseases, Osaka University, Osaka, Japan. [6]Department of Gastroenterology and Hepatology, Osaka University, Osaka, Japan. [7]Division of Molecular Genetics, Cancer Research Institute, WPI Nano Life Science Institute, Kanazawa University, Kanazawa, Japan. [8]Center for Lung Regenerative Medicine, Division of Pulmonary Biology, Cincinnati Children's Hospital Medical Center, Cincinnati, OH, USA. *e-mail: mishii@icb.med.osaka-u.ac.jp

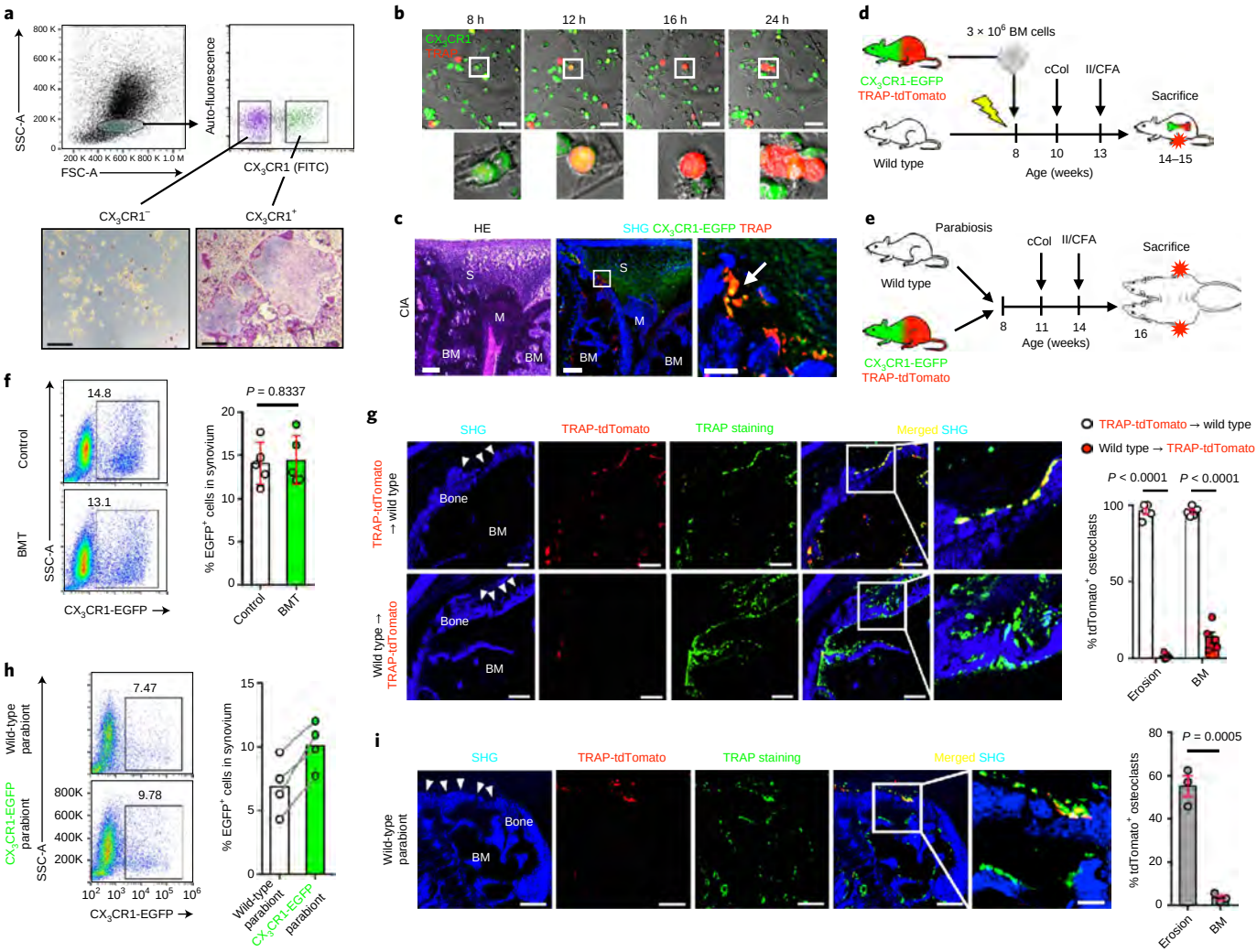

Fig. 1 | BM-derived CX$_3$CR1$^+$ cells differentiate into osteoclasts in pannus. a, In vitro differentiation of CX$_3$CR1$^+$ cells isolated from inflamed synovium of knee joints into osteoclast-like cells on RANKL stimulation. Scale bars: 100 µm. Data are representative of three independent experiments with similar results. **b**, Ex vivo incubation of inflamed synovium of knee joints from double-transgenic mice (CX$_3$CR1-EGFP and TRAP-tdTomato) on RANKL stimulation. The bottom row show enlargements of the areas shown by a white box in the images above. Scale bars: 50 µm. Images are representative of two independent experiments with similar results. **c**, Representative confocal images of arthritic knee joints from CX$_3$CR1-EGFP transgenic mice with TRAP staining. The right image shows enlargement of the area outlined in white in the middle image. The arrow indicates merged osteoclasts. M, meniscus; S, synovium. Scale bars: 200 µm (left and middle images) and 30 µm (right image). Images are representative of two independent experiments with similar results. HE, hematoxylin and eosin. **d**,**e**, Schematics showing the experimental design for BM chimeric mice (**d**) and parabiotic mice (**e**) with CIA. **f**, Flow cytometry plots (left) and cumulative data (right) of CX$_3$CR1-EGFP$^+$ cells (as a proportion of CD45$^+$ cells) from inflamed knee joints of CX$_3$CR1-EGFP transgenic mice (control) and BM chimeric mice (BMT) ($n = 5$ mice per group). **g**, Representative confocal images (left) and frequencies (right) of TRAP-tdTomato$^+$ osteoclasts among TRAP staining$^+$ osteoclasts in the inflamed knee joints of the indicated chimeras. Arrowheads indicate the site of bone erosion. Scale bars: 200 µm ($n = 5$ mice for each group). **h**, Flow cytometry plots (left) and cumulative data (right) of CX$_3$CR1-EGFP$^+$ cells (as a proportion of CD45$^+$ cells) from inflamed knee joints of the indicated parabionts ($n = 4$ mice per group). **i**, Representative confocal images (left) and frequencies (right) of TRAP-tdTomato$^+$ osteoclasts among TRAP staining$^+$ osteoclasts in the inflamed knee joints of indicated parabionts. Scale bars: 150 µm (left four images) and 50 µm (right image) ($n = 3$ mice per group). Statistical significance was determined by unpaired two-tailed *t*-test (**f**, **g** and **i**). Means ± s.e.m. for each group are shown. Symbols represent individual mice.

inflamed ankle joint synovium was possible (Supplementary Fig. 1c,d). CX$_3$CR1—a fractalkine receptor and marker for monocyte-lineage cells including an osteoclast precursor-containing population in BM (BM-OPs) under homeostatic conditions[8,13,14]—was also able to mark osteoclast precursors in the inflamed synovium in vitro (Fig. 1a). We then backcrossed CX$_3$CR1-enhanced green fluorescent protein (EGFP) knock-in mice and tartrate-resistant acid phosphatase (TRAP)-tdTomato transgenic mice onto the DBA/1J background to develop a reporter system for osteoclast differentiation in this model system. Ex vivo incubation of the inflamed synovium from double-transgenic mice (CX$_3$CR1-EGFP/TRAP-tdTomato) showed that EGFP$^+$ cells gradually expressed tdTomato and underwent cell fusion to differentiate into osteoclasts, followed by a loss of CX$_3$CR1 expression (Fig. 1b and Supplementary Video 1). CX$_3$CR1$^+$TRAP$^+$ cells that were in transition from osteoclast precursors to osteoclasts were detected at the pannus–bone interface in tissue sections (Fig. 1c). Together, these results suggest that EGFP$^+$ cells in the synovium contain osteoclast precursors associated with arthritis.

As synovium-resident macrophages expressed CD11b[15] and CX$_3$CR1-EGFP (Supplementary Fig. 2a,b), we used BM chimeric

mice with CX_3CR1-EGFP and TRAP-tdTomato hematopoietic cells to determine whether osteoclasts at the pannus–bone interface originate from the proliferation of local CX_3CR1^+ macrophages or newly recruited blood monocytes from BM. We used a nonlinear optical process—second-harmonic generation (SHG)—to distinguish synovial lining cells from BM cells by visualizing collagen-enriched bone matrices and synovial fibrous tissues (Supplementary Fig. 2a). After confirming that local $EGFP^+$ macrophages were radio-resistant (Supplementary Fig. 2c–e) and <15% were replaced by BM cells 6 weeks after transplantation (Supplementary Fig. 2f–h), we induced CIA in the chimeric mice (Fig. 1d). The $EGFP^+$ cell frequencies in the inflamed synovium were equivalent between chimeric mice and control mice (Fig. 1f). Counting the frequencies of $tdTomato^+$ osteoclasts among total osteoclasts labeled by TRAP staining in wild-type mice transplanted with BM cells of TRAP-tdTomato transgenic mice revealed that >95% of the osteoclasts at the pannus–bone interface were derived from BM (Fig. 1g). Furthermore, an analysis of parabiotic mice involving wild-type and double-transgenic (CX_3CR1-EGFP and TRAP-tdTomato) mice paired for up to 2 months showed that >40% of blood CX_3CR1^+ monocytes were exchanged between parabionts, although <3% of synovial CX_3CR1^+ macrophages were exchanged under these physiological conditions (Supplementary Fig. 2i–k). When CIA was induced in both parabionts (Fig. 1e), $EGFP^+$ cells and $tdTomato^+$ osteoclasts were detected in pannus from wild-type parabionts, supporting the idea that the CX_3CR1^+ osteoclast precursors and osteoclasts in pannus originated from cells in the blood circulation (Fig. 1h,i).

$CX_3CR1^{hi}Ly6C^{int}F4/80^{hi}I\text{-}A^+/I\text{-}E^+$ macrophages in inflamed synovium have high osteoclast differentiation potential. To more specifically identify the subset origin of CX_3CR1^+ osteoclast precursors, we performed a flow cytometric analysis of cells from the blood, BM and synovium of mice with CIA 1 week after the onset of arthritis. The frequencies and numbers of $CX_3CR1^{lo}Ly6C^{hi}$ cells (called 'inflammatory monocytes')[16] were significantly increased in the blood and BM of mice with CIA (Fig. 2a,b). The inflamed synovium of mice with CIA contained $CX_3CR1^{lo}Ly6C^{hi}$ cells, whereas $CX_3CR1^{hi}Ly6C^-$ cells (called patrolling monocytes)[16] were absent (Fig. 2c). There was a $CX_3CR1^{hi}Ly6C^{int}$ subset only in the CIA synovium. Because our chimeric data showed that the CX_3CR1^+ cells were almost all derived from blood, it is likely that $CX_3CR1^{lo}Ly6C^{hi}$ cells in the blood (R1) trans-migrated into the synovium (R2) and then differentiated into $CX_3CR1^{hi}Ly6C^{int}$ cells (R3) in situ (Fig. 2d). Indeed, inflamed synovium in wild-type parabionts, conjoined with CX_3CR1-EGFP mice, contained R3 cells, suggesting that such cells originated from a circulating population (Fig. 2e). Furthermore, when isolated R2 cells were labeled with CellTrace Violet and transferred into the inflamed knee joints of wild-type mice, >70% of the transferred R2 cells differentiated into R3 cells (Fig. 2f). These results are consistent with our suggestion that R1 cells in the blood enter the inflamed synovium (R2) and differentiate into R3 cells. A phenotypic analysis revealed that the R3 cells were relatively large, $F4/80^{hi}$, $I\text{-}A^+/I\text{-}E^+$, $CD11c^{lo}$ and $RANK^{dim}$, and distinct from the BM-OPs that have been characterized as being within the $CX_3CR1^+Ly6C^{hi}F4/80^+$ fraction[8,13] (Fig. 2g and Supplementary Fig. 3a). The R3 subset was sparse in other organs under both healthy and inflamed conditions, such as dextran sulfate sodium (DSS)-induced colitis (Supplementary Fig. 3b), suggesting that the R3 subset is tissue restricted in its distribution, with a high abundance in the inflamed synovium. Because R2 cells differentiate gradually into R3 cells in situ, both R2 and R3 fractions may contain transitional states. In fact, R2 and R3 cells constitute heterogeneous populations, at least in terms of cellular size and granularity (as reflected by the FSC (forward scatter)/SSC (side scatter)); based on the F4/80 expression, we newly defined R3′ ($CX_3CR1^{hi}Ly6C^{int}F4/80^{hi}$) as 'fully differentiated R3' for further analyses (Supplementary Fig. 4a). Similarly, we defined R2′ ($CX_3CR1^{lo}Ly6C^{hi}F4/80^{int}$) as 'basal state R2'. May–Giemsa staining showed that the R3′ cells had an abundant foamy cytoplasm and cytoplasmic vacuoles, representing a macrophage morphology (Fig. 2h). In contrast, R2′ cells had peripherally located kidney-shaped nuclei, indicating that differentiation to the macrophage state is not obligatory for monocytes after entry into the synovium without an additional trigger. When stimulated directly with RANKL, R3′ cells readily differentiated into osteoclasts that resorbed inorganic crystalline calcium phosphate in vitro (Fig. 2i), suggesting that R3′ cells contain functional osteoclast precursors in the inflamed synovium; therefore, we designated these cells as AtoMs. The proportion and osteoclastogenic potential of R3 cells were comparable in the knee and ankle joints (Supplementary Fig. 4b,c). Although the BM also contained a small population of $CX_3CR1^{hi}Ly6C^{int}$ cells with the potential to form osteoclasts, May–Giemsa staining of these cells showed cells with diameters of 8–12 μm and peripherally located kidney-shaped nuclei (Supplementary Fig. 3c,d), which is the characteristic monocyte morphology. This is explained by a previous observation that $CX_3CR1^{hi}Ly6C^-$ monocytes are derived from $CX_3CR1^{lo}Ly6C^{hi}$ monocytes in the BM[17], and $CX_3CR1^{hi}Ly6C^{int}$ cells in the BM may be in transition from $Ly6C^{hi}$ monocytes to $Ly6C^-$ monocytes, indicating that $CX_3CR1^{hi}Ly6C^{int}$ cells in the BM are distinct from inflamed synovium R3 cells.

The RANKL–RANK–OPG axis is essential for R3′ cell osteoclastogenesis. Previous studies reported that tumor necrosis factor (TNF) and interleukin-6 (IL-6) drive osteoclast formation in BM-derived macrophages (BMMs) in vitro, suggesting the presence of a RANKL-independent pathway of osteoclastogenesis[18,19]. Therefore, we examined whether R3′ cells from the inflamed synovium can differentiate into osteoclasts without RANKL. The results showed that TNF and IL-6 minimally induced osteoclasts from R3′ cells compared with RANKL (Fig. 3a,b). In contrast, the simultaneous addition of TNF and RANKL significantly promoted RANKL-induced osteoclastogenesis (Fig. 3a,b). Previous studies showed that TNF did not enhance osteoclastogenesis in BMMs when added simultaneously with RANKL. However, RANKL priming several days before the addition of TNF induced maximum osteoclastogenesis[20,21]. Collectively, these results imply that R3′ cells were already primed by RANKL in the pannus microenvironment. Furthermore, IL-6 was reported to trigger osteoclast formation together with soluble IL-6 receptor in BM cells[22]. However, IL-6 partially inhibited RANKL-induced osteoclastogenesis of R3′ cells (Fig. 3a,b). Considering that RANKL–RANK signaling is essential for osteoclastogenesis of R3′ cells, we examined the effect of the decoy receptor osteoprotegerin (OPG), which showed dose-dependent inhibition of osteoclastogenesis induced by RANKL or RANKL plus TNF (Fig. 3c,d). Together, simultaneous stimulation of RANKL and TNF most efficiently induced osteoclast formation of R3′ cells, and the RANKL–RANK–OPG axis is essential for their osteoclastogenesis.

Transcriptional profiling by RNA sequencing (RNA-Seq) identifies FoxM1 as one of the key regulators of R3′ cells. Next, we performed an unbiased global transcriptomic comparison of R1, R2′ and R3′ cells by RNA-Seq. Principal component analysis showed tight clustering across replicates, indicating that R1–R3′ cells constitute distinct, reproducible subsets (Fig. 4a). Based on the top 300 upregulated genes, we found that R2′ cells had higher expression of transcripts encoding chemokines (*Cxcl1*, *Cxcl2*, *Ccl2*, *Ccl3* and *Ccl4*), inflammatory cytokines (*Il1*, *Il6* and *Tnf*) and *Vegfa* than R1 cells (Fig. 4b). In contrast, R3′ cells showed preferential expression of osteoclast marker genes (*Ctsk*, *Acp5*, *Mmp9*, *Atp6v0d2* and *Ppargc1b*) (Fig. 4c,d), and a gene set enrichment analysis (GSEA) showed the enrichment of genes associated with osteoclast

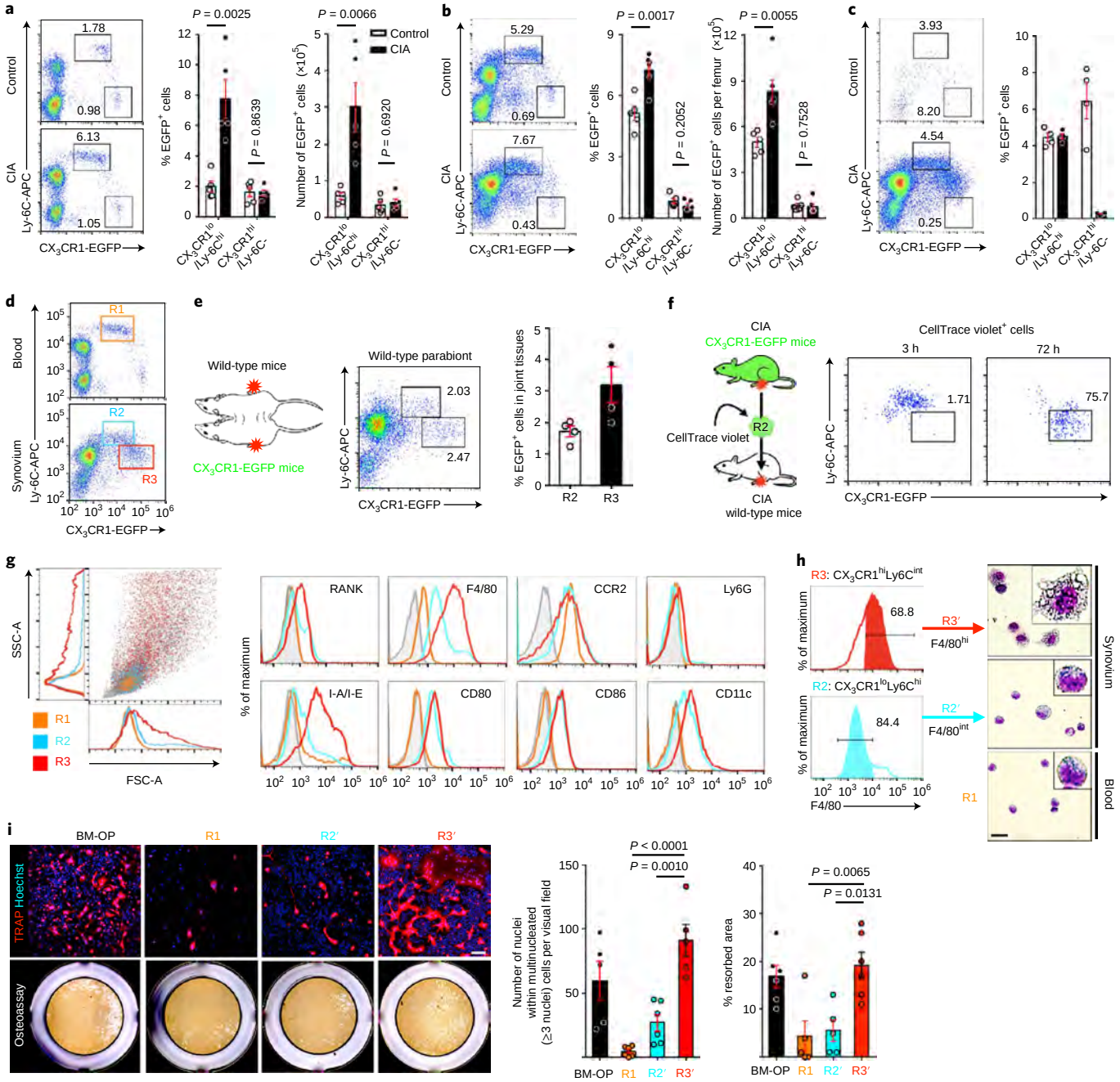

Fig. 2 | $CX_3CR1^{hi}Ly6C^{int}F4/80^{hi}I\text{-}A^+/I\text{-}E^+$ macrophages in the inflamed synovium have high osteoclast differentiation potential. a–c, Representative plots (left) and quantification (right) of $CX_3CR1\text{-}EGFP^+$ cells (as a proportion of $CD45^+$ cells) in the blood (**a**), BM (**b**) and joints (**c**) of control mice and mice with CIA 1 week after arthritis onset ($n = 5$ mice for both groups **a** and the control group in **b**; $n = 6$ mice for the CIA group in **b**; and $n = 4$ mice for both groups in **c**). In **a** and **b**, numbers of cells are shown in addition to percentages. **d**, Definitions of R1, R2 and R3 cells in the blood and synovium of mice with CIA. **e**, Detection of R2 and R3 cells in the CIA knee synovium of wild-type parabionts paired with $CX_3CR1\text{-}EGFP$ transgenic mice ($n = 4$ mice). **f**. Adoptive transfer of CellTrace Violet-labeled R2 cells from the inflamed knee synovium of $CX_3CR1\text{-}EGFP$ transgenic mice into the inflamed knee joints of wild-type mice. Data are representative of three independent experiments with similar results. **g**, Flow cytometry-based phenotypic characterization of R1, R2 and R3 cells with the indicated cell-surface markers. Shaded regions indicate staining with isotype controls. Dot plots of FSC-A (forward scatter)/SSC-A (side scatter) are displayed with an overlay of R1 cells from blood, as well as R2 and R3 cells from synovium. Data are representative of three independent experiments with similar results. **h**, Morphological assessment of R1, R2′ and R3′ cells with May–Giemsa staining. Scale bar: 20 µm. Images are representative of two independent experiments with similar results. **i**, Osteoclast differentiation (top left) and resorption potential (bottom left) of R1, R2′ and R3′ cells and BM-OPs. R1, R2′ and R3′ cells and BM-OPs were sorted and directly stimulated with 100 ng ml^{-1} RANKL and 10 ng ml^{-1} M-CSF for 6 d. In calculating the number of nuclei within osteoclasts, $n = 5$ mice for the BM-OP and R3′ groups, and $n = 6$ mice for the R1 and R2′ groups. In calculating the % resorbed area, $n = 6$ mice for the BM-OP and R3′ groups, and $n = 5$ mice for the R1 and R2′ groups. Significance was determined by unpaired two-tailed *t*-test (**a** and **b**) and one-way ANOVA with Bonferroni's post-hoc test (**i**). Data represent means ± s.e.m. for each group. Symbols represent individual mice, except for the control group in **c**, where multiple mice were used for a single symbol because of the limited number of cells in the uninflamed condition.

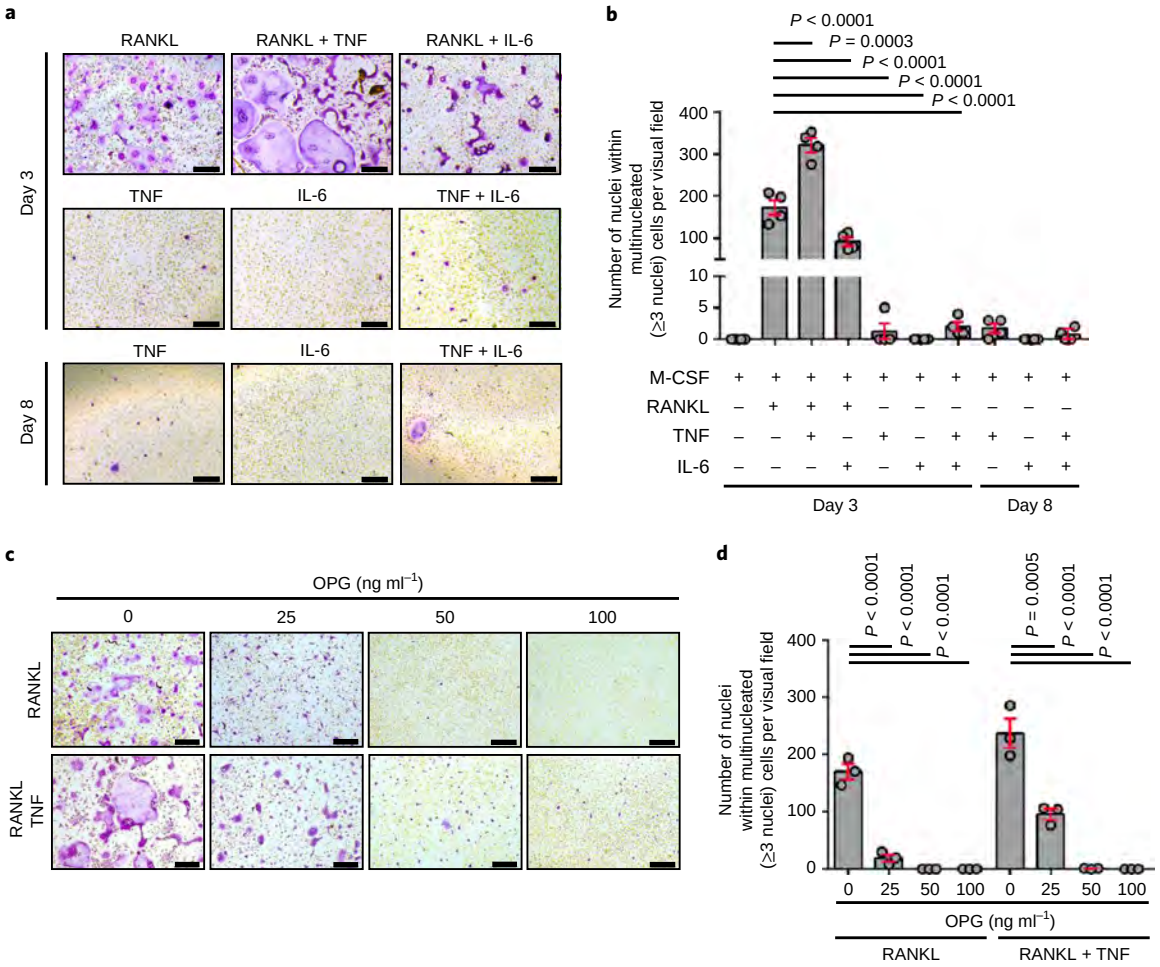

Fig. 3 | The RANKL–RANK–OPG axis is essential for R3′ cell osteoclastogenesis. a. Representative TRAP staining images of synovial R3′ cells from knee and ankle joints cultured with 10 ng ml^{-1} M-CSF, 50 ng ml^{-1} RANKL, 50 ng ml^{-1} TNF or 50 ng ml^{-1} IL-6, either alone or in combination. Scale bars: 200 µm. **b**, Quantification of nuclei within multinucleated cells within the visual field in **a** ($n = 4$ mice per group). **c**, Representative TRAP staining images of R3′ cells cultured with 10 ng ml^{-1} M-CSF, 50 ng ml^{-1} RANKL and 50 ng ml^{-1} TNF, with OPG at the indicated concentrations. Scale bars: 200 µm. **d**, Quantification of nuclei within multinucleated cells within the visual field in **c** ($n = 3$ mice per group). Statistical significance was determined by one-way ANOVA with Bonferroni post-hoc test (**b** and **d**). Data represent means ± s.e.m. for each group. Symbols represent individual mice.

differentiation, mitochondrial translation and oxidative phosphorylation, compared with R2′ cells (Fig. 4e, Supplementary Fig. 4d and Supplementary Table 1). To determine the transcription factors responsible for regulating the osteoclastogenic potential of R3′ cells, we generated a global messenger RNA (mRNA) expression profile of transcription factors increased in the R3′ subset, and predicted upstream regulators with QIAGEN's Ingenuity Pathway Analysis. The predicted regulator with the top *z* score was *Foxm1* (Fig. 4f and Supplementary Fig. 4e), which was increased by 11.69-fold. This upregulation was validated at both the mRNA and protein levels (Fig. 4g,h). *E2f1*—a transcription factor that was reported previously to promote osteoclastogenesis under inflammatory conditions[23]—was detected as a predicted regulator with the second-highest *z* score.

FoxM1 is a multifaceted transcription factor with diverse and cell type-specific functions in vivo[24]. In adult tissues, FoxM1 plays a prominent role in carcinogenesis by inducing the epithelial–mesenchymal transition—a process that renders tumor cells more aggressive and invasive[24], leading to metastasis[25]. Because the invasive phenotype of a tumor is analogous to pannus in arthritis, which erodes the bone surface to destroy joints, these correlations prompted us to explore the function of FoxM1 in arthritis. A natural product—thiostrepton—interacts directly with FoxM1 and inhibits its binding to genomic target sites[26]. Thiostrepton also prevents FoxM1 from binding to and activating its own promoter, disrupting the positive auto-regulatory loop[27] without being cytotoxic in untransformed cells[28]. The treatment of R3′ cells with thiostrepton resulted in the efficient attenuation of *Foxm1* expression in a dose-dependent manner (Fig. 4i) without inducing apoptosis or inhibiting cell proliferation at concentrations of ≤1 µM (Supplementary Fig. 5a,b). Thiostrepton inhibited the osteoclastogenesis of R3′ cells significantly in vitro (Fig. 4j), and attenuated articular bone erosion in vivo (Fig. 4l,m). Thiostrepton partially reduced the arthritic scores of mice with CIA (Fig. 4k) and inhibited inflammatory cytokine expression in the synovium (Supplementary Fig. 5c), which may indirectly protect against bone erosion. To elucidate the effect of thiostrepton on homeostatic bone remodeling, we injected 50 mg kg^{-1} thiostrepton twice a week for 5 weeks. Body growth and bone morphology did not differ between vehicle- and thiostrepton-treated groups, indicating that thiostrepton does not affect homeostatic bone remodeling in vitro or in vivo (Supplementary Fig. 5d–h). These results show that FoxM1 is involved in the osteoclastogenic potential of R3′ cells in arthritis.

Single-cell RNA-Seq analysis identifies highly osteoclastogenic population in synovial R3 cells. Since only a portion of

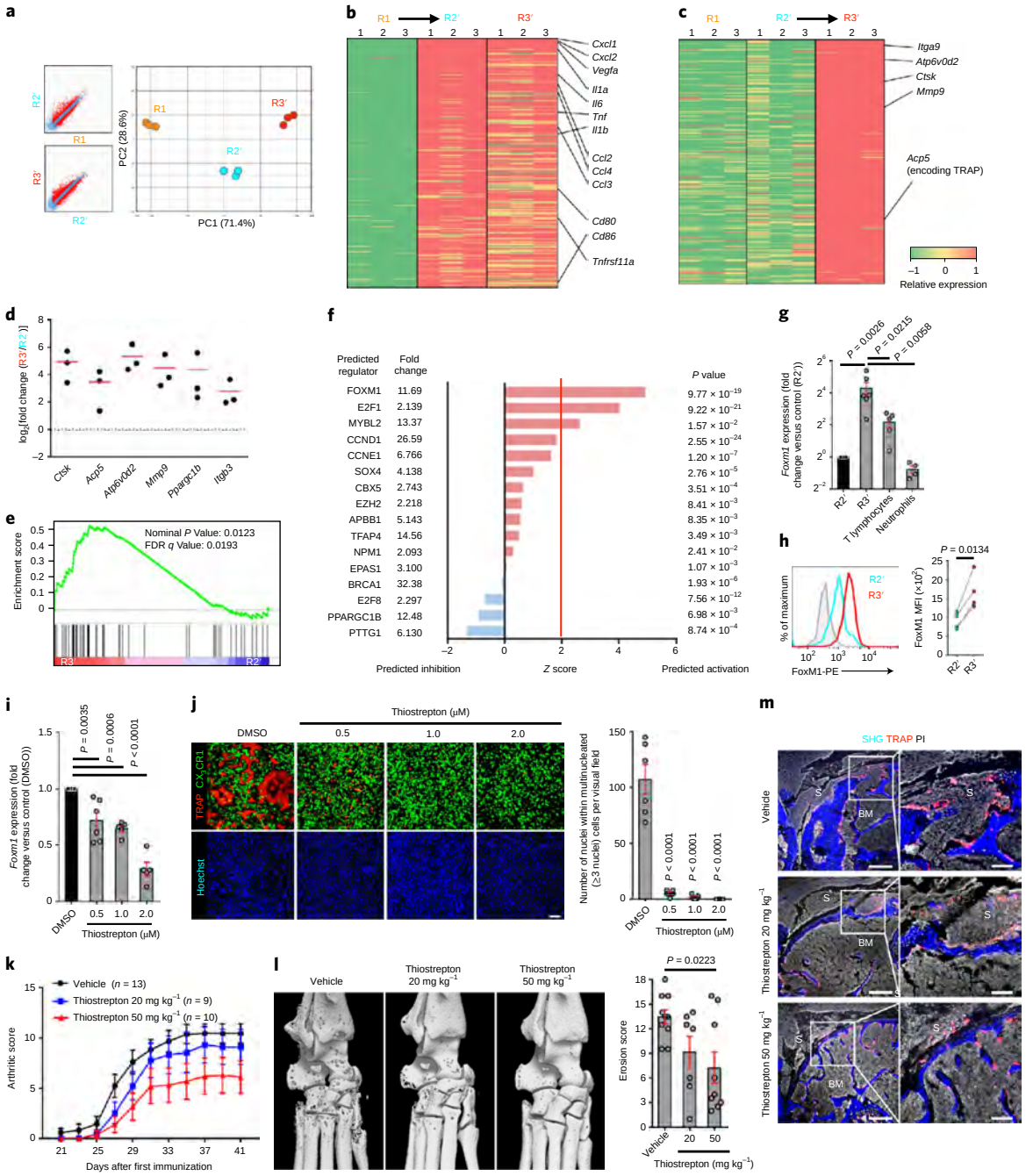

Fig. 4 | Transcriptional profiling by RNA-Seq identifies FoxM1 as a key regulator of R3′ cells. a, Scatter plot analysis (left) and principal component analysis (right) of R1, R2′ and R3′ cells by RNA-Seq ($n=3$ mice for the R1, R2′ and R3′ populations). **b**,**c**, Heatmaps of the top 300 upregulated genes from R1 to R2′ cells (**b**) and from R2′ to R3′ cells (**c**). **d**, Expression analysis of osteoclast marker genes in R3 cells. Values indicate the fold change of FPKM in R3′/R2′ cells ($n=3$ mice for the R2′ and R3′ populations). Horizontal bars represent mean values. **e**, Enrichment analysis of osteoclast differentiation and fusion genes in R3′ cells compared with R2′ cells ($n=3$ mice for the R2′ and R3′ populations). FDR, false discovery rate. **f**, Upstream regulator analysis of differentially expressed genes among upregulated transcription factors in R3′ ($n=3$ mice for the R2′ and R3′ populations). Red vertical line indicates a *Z*-score of 2 (significant activation). **g**, RT-PCR analysis of *Foxm1* expression in R2′ cells, R3′ cells, T lymphocytes and neutrophils from the inflamed synovium ($n=6$ mice for R2′ and R3′; $n=5$ mice for T lymphocytes; and $n=4$ mice for neutrophils). **h**, Representative histogram plots (left) and quantitative mean fluorescence intensity (MFI) (right) of FoxM1 in R2′ and R3′ cells. Shaded regions indicate staining with isotype control ($n=4$ mice per group). **i**, RT-PCR analysis of *Foxm1* expression in R3′ cells after incubation with thiostrepton for 48 h ($n=6$ mice for dimethyl sulfoxide (DMSO) and 0.5 μM thiostrepton; and $n=5$ mice for 1 and 2 μM thiostrepton). **j**, Inhibition of RANKL-induced osteoclastogenesis of R3′ cells by thiostrepton. Scale bar: 100 μm ($n=6$ mice for DMSO and 2 μM thiostrepton; and $n=5$ mice for 0.5 and 1 μM thiostrepton). **k**, Clinical arthritic scores of mice with CIA treated with vehicle, 20 mg kg^{-1} thiostrepton or 50 mg kg^{-1} thiostrepton. **l**, Representative 3D reconstructions and erosion scores of the rear paws by micro-CT analysis ($n=10$ mice for vehicle; $n=7$ mice for thiostrepton 20 mg kg^{-1}; and $n=9$ mice for thiostrepton 50 mg kg^{-1}). **m**, Histological examination of inflamed knee joints. Images are representative of at least three similar experiments. Scale bars: 300 μm (left) and 100 μm (right). Cells were stained with propidium iodide (PI). Statistical significance was determined by paired two-tailed *t*-test (**h**), one-way ANOVA with Bonferroni's post-hoc test (**g**, **i**, **j** and **l**), Kolmogorov–Smirnov statistic (**e**) or Fisher's exact test (**f**). Data represent means ± s.e.m. for each group. Symbols represent individual mice.

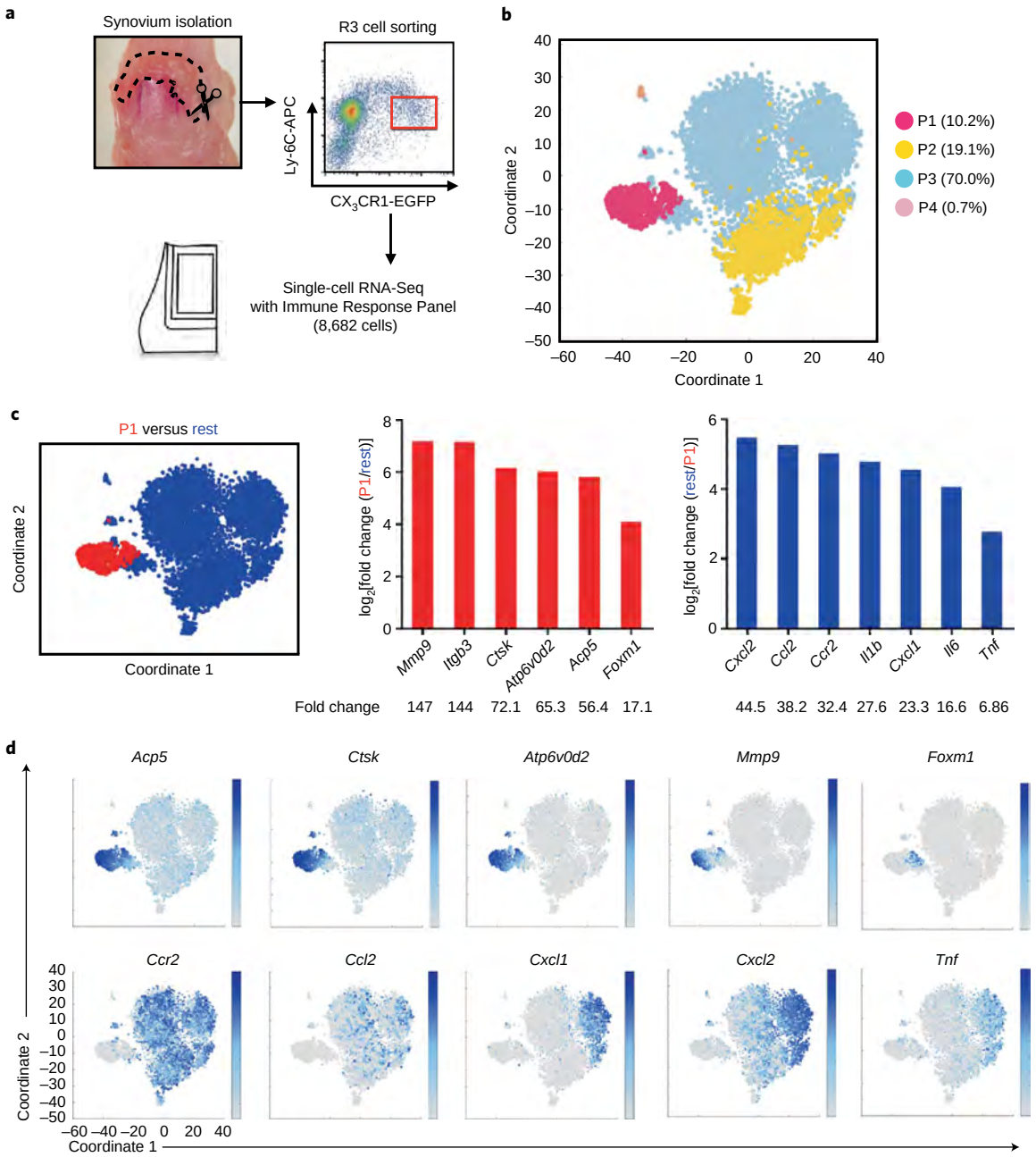

Fig. 5 | Single-cell RNA-Seq analysis of synovial R3 cells. a, Schematic outlining the single-cell RNA-Seq analysis. R3 cells were isolated from inflamed knee synovium 1 week after CIA onset. **b**, t-SNE plot of the single-cell RNA-Seq data of 8,682 R3 cells from mice with CIA. Hierarchical clustering based on gene expression profiles was performed using BD DataView software. **c**, Differential expression analysis of cluster P1 and the other cell clusters. Fold changes were calculated for differentially expressed genes. The cell numbers of the 'P1' and 'rest' groups analyzed were 784 and 1,461 (*Mmp9*), 652 and 255 (*Itgb3*), 885 and 6,011 (*Ctsk*), 885 and 1,098 (*Atp6v0d2*), 886 and 6,093 (*Acp5*), 258 and 241 (*Foxm1*), 239 and 5,685 (*Cxcl2*), 77 and 3,709 (*Ccl2*), 138 and 6,883 (*Ccr2*), 14 and 1,395 (*Il1b*), 107 and 2,662 (*Cxcl1*), 4 and 98 (*Il6*), and 180 and 3,791 (*Tnf*), respectively. **d**, Single-gene expression plots on the t-SNE plot of the single-cell RNA-Seq data.

inflamed synovium cells differentiate into osteoclasts in vivo, we hypothesized the presence of a specific subpopulation in R3 cells, which is in transition from osteoclast precursors to osteoclasts on articular bone surfaces. To identify and characterize the population, we sorted R3 cells from inflamed knee synovium 1 week after CIA onset and conducted single-cell RNA-Seq analysis (Fig. 5a). A total of 8,682 R3 cell transcriptomes were analyzed and hierarchically clustered using t-distributed stochastic neighbor embedding (t-SNE) (Fig. 5b). Among the four R3 cell clusters, P1 exhibited the osteoclastogenic phenotype, constituting 10.2% of R3 cells. The expression levels of osteoclast-related genes, such as *Acp5* (encoding TRAP), *Ctsk*, *Atp6v0d2*, *Mmp9* and *Itgb3*, were, respectively, 56.4, 72.1, 65.3, 147 and 144 times higher in the P1 cluster compared with the rest of the cell clusters (Fig. 5c,d). Chemokines, chemokine receptors and inflammatory cytokines, such as *Tnf*, were preferentially expressed in the other clusters relative to P1 (Fig. 5c,d). The expression level of *Foxm1* was 17.1 times higher in P1 compared with the other clusters, supporting its role as a regulator of osteoclastogenesis in a specific cell type of the inflamed synovium (Fig. 5c,d).

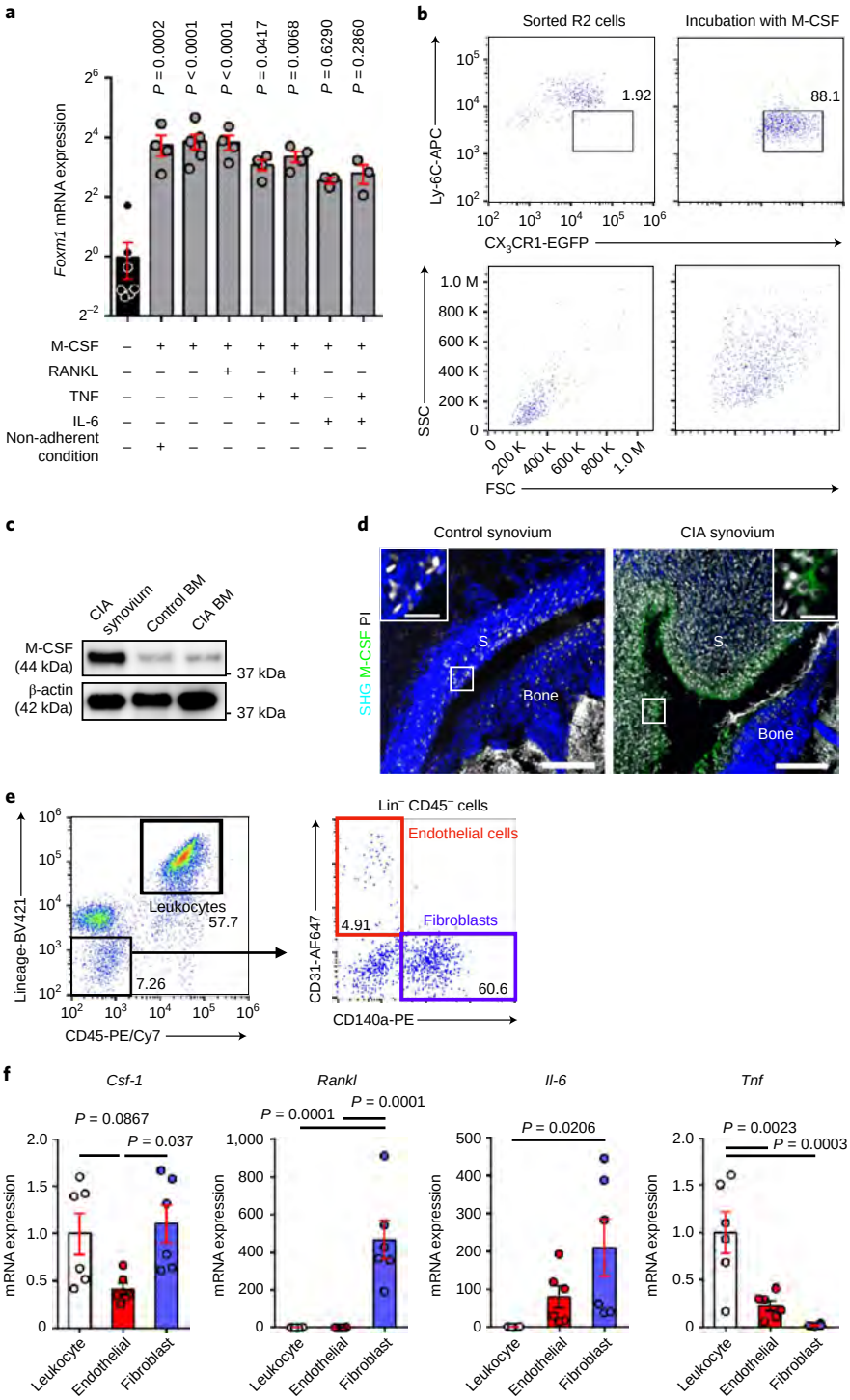

Fig. 6 | M-CSF mediates R2 to R3 cell transition. a, *Foxm1* RT-PCR analysis in flow cytometry-sorted R2 cells from inflamed knee joints after incubation with the indicated cytokines for 72 h (concentrations of 10 ng ml^{-1} M-CSF, 100 ng ml^{-1} RANKL, 100 ng ml^{-1} TNF and 100 ng ml^{-1} IL-6). Expression is shown relative to β-actin. Nunclon Sphera plates were used for the non-adherent condition. For the M-CSF (−) group, R2 cells were sorted and directly examined by RT-PCR analysis ($n = 7$ mice for no M-CSF; $n = 6$ mice for M-CSF; $n = 4$ mice for the M-CSF + non-adherent condition, M-CSF + RANKL, M-CSF + TNF and M-CSF + TNF + RANKL; and $n = 3$ mice for M-CSF + IL-6 and M-CSF + TNF + IL-6). **b**, Representative plots of flow cytometry-sorted R2 cells from inflamed knee joints before and after incubation with 10 ng ml^{-1} M-CSF. Similar results were obtained in three independent experiments. **c**, M-CSF western blot analysis of CIA synovium, control BM and BM from mice with CIA. Images are representative of two independent experiments with similar results. **d**, Representative confocal images of control and CIA knee synovium. Images are representative of two experiments with similar results. Scale bars, 100 and 20 μm (enlarged images). Cells were stained with propidium iodide (PI). **e**, Gating strategy for leukocytes (Lin$^+$CD45$^+$ cells), endothelial cells (Lin$^-$CD45$^-$CD31$^+$CD140a$^-$ cells) and fibroblasts (Lin$^-$CD45$^-$CD140a$^+$CD31$^-$ cells) in the inflamed synovium of mice with CIA. **f**, *Csf1*, *Rankl*, *Il6* and *Tnf* RT-PCR analyses in flow cytometry-sorted leukocytes, endothelial cells and fibroblasts, according to the protocol in **e** ($n = 6$ mice per group). Expression is shown relative to β-actin. Statistical significance was determined by one-way ANOVA with Bonferroni's post-hoc test (**a** and **f**). Data represent means ± s.e.m. for each group. Symbols represent individual mice.

M-CSF mediates R2 to R3 cell transition. To identify the cytokine(s) responsible for the transition from R2 to R3 cells and upregulation of *Foxm1* expression, we sorted R2 cells from the inflamed synovium, then incubated them with M-CSF and RANKL (the cytokines essential for osteoclastogenesis[5,6,29,30]) or inflammatory cytokines, such as TNF and IL-6. The results showed that M-CSF alone upregulated *Foxm1* expression (Fig. 6a) and triggered differentiation into R3 cells (Fig. 6b), potentially explaining the protective effect of an M-CSF deletion on bone erosion in arthritis[31,32]. In contrast, RANKL, TNF, IL-6 and the combination of TNF plus IL-6 had no additive effect with M-CSF, and adhesion was dispensable for *Foxm1* upregulation (Fig. 6a). Consistent with previous studies showing that inflammatory cytokines stimulate the production of M-CSF from synovial fibroblasts[33], chondrocytes[34] and endothelial cells[35], the M-CSF expression levels were higher in inflamed synovium than in BM and healthy synovium, signifying an arthritis-specific environment that could promote erosive events (Fig. 6c,d). Although overexpression of *Foxm1* did not induce spontaneous osteoclast formation (Supplementary Fig. 6a–c), the minimum dose of M-CSF required for RANKL-induced osteoclastogenesis was lower in macrophages overexpressing *Foxm1*, supporting its role in partially replacing the contribution of M-CSF to osteoclastogenesis (Supplementary Fig. 6d,e).

The source of key cytokines in inflamed synovium was further examined by isolating leukocytes (Lin^+CD45^+ cells), endothelial cells ($Lin^-CD45^-CD31^+CD140a^-$ cells) and fibroblasts ($Lin^-CD45^-CD140a^+CD31^-$ cells) from CIA synovium (Fig. 6e). The expression of *Csf1* (encoding M-CSF) was higher in fibroblasts and leukocytes compared with endothelial cells, while *Rankl* expression in fibroblasts was about 400 times higher than in leukocytes and endothelial cells (Fig. 6f). Among inflammatory cytokines, the expression of *Il6* was highest in fibroblasts, and *Tnf* was highest in leukocytes (Fig. 6f).

Next, we examined whether *Foxm1* expression levels differ between R3 cells and mature osteoclasts. Approximately 40% of the R3 cells seeded on the plate differentiated into osteoclasts (Supplementary Fig. 6f). Resultant mononuclear cells and multinucleated mature osteoclasts were isolated from the temperature-responsive cell cultureware, RepCell (Supplementary Fig. 6g), and $FSC^{hi}SSC^{hi}$TRAP-tdtomato$^+$ multinucleated osteoclasts were sorted as described previously[10], with slight modifications (Supplementary Fig. 6h). *Foxm1* expression was comparable between R3 cells and mature osteoclasts (Supplementary Fig. 6i), indicating that multinucleation does not upregulate *Foxm1* expression.

FoxM1 contributes to arthritis-induced bone destruction. Next, we analyzed the effects of the *Foxm1* time-specific deletion in $Foxm1^{fl/fl}Rosa26^{CreERT2}$ mice. Since C57BL/6 (B6) mice were resistant to reliable CIA induction, we used the collagen antibody-induced arthritis (CAIA) model. We found that R3′ cells also developed under these conditions (Supplementary Fig. 6j,k), and that arthritis was consistently induced in B6 mice[36]. The in vivo injection of tamoxifen efficiently deleted *Foxm1* genes (Fig. 7a,b) and suppressed *Foxm1* expression in leukocytes including CX_3CR1^+ macrophages (Fig. 7c). *Foxm1* deletion partially inhibited synovial R3 cell osteoclastogenesis in vitro (Fig. 7d) without inducing apoptosis (Fig. 7e) or altering TNF expression (Fig. 7f). *Foxm1* deletion mitigated bone erosion in vivo, which was partly reversed by the adoptive transfer of $Foxm1^{+/+}CX_3CR1^+$ monocytes (but not by $Foxm1^{-/-}CX_3CR1^+$ monocytes (Fig. 7g,i–k)), and partially reduced the arthritic score (Fig. 7h). In contrast, osteoclastogenesis by BM-OPs was not affected by *Foxm1* deletion in vitro (Fig. 7d). Myeloid cell-specific *Foxm1* knockout mice ($Foxm1^{fl/fl}$*Lyz2*-cre) and global deletion beginning at 6 weeks of age resulted in no change in body growth or physiological bone remodeling (Supplementary Fig. 7a–g).

To clarify the role of FoxM1 in the conversion of R2 cells into R3 cells, we sorted R2 cells from CAIA mice treated with or without tamoxifen (Supplementary Fig. 7h). Incubation with M-CSF successfully converted R2 cells into R3 cells in both groups ($Foxm1^{+/+}$ and $Foxm1^{-/-}$), indicating that FoxM1 is dispensable for upregulation of CX_3CR1 and downregulation of Ly6C (Supplementary Fig. 7i).

Rheumatoid arthritis synovial $CX_3CR1^+HLA\text{-}DR^{hi}CD11c^+CD86^+$ cells have high osteoclastogenic potential. Finally, we examined the relevance of the osteoclastogenesis mechanism in humans. We used CX_3CR1 and HLA-DR to identify the subset with high osteoclastogenic potential. We detected $CX_3CR1^+HLA\text{-}DR^{hi}CD14^+CD64^+$ cells in the synovial fluid and synovium, but not in the blood, of patients with rheumatoid arthritis (Fig. 8a and Supplementary Fig. 8). Given that these cells from the synovial fluid and synovium of patients with rheumatoid arthritis were negative for CD80, positive for CD11c and partially positive for CD86 (Fig. 8b), we further divided $CX_3CR1^+HLA\text{-}DR^{hi}$ cells into $CX_3CR1^+HLA\text{-}DR^{hi}CD11c^+CD86^-$ cells (P1) and $CX_3CR1^+HLA\text{-}DR^{hi}CD11c^+CD86^+$ cells (P2) (Fig. 8c). P2 cells had higher potential for osteoclast formation and *Foxm1* expression compared with P1 cells (Fig. 8d,e), and thiostrepton significantly inhibited osteoclastogenesis by these cells (Fig. 8f). Because P1 and P2 cells express CD86 over a continuous range of values, without a clear threshold separating distinct subpopulations, some of the P1 cells with relatively high *Foxm1* expression also formed osteoclasts (Fig. 8g), and this was inhibited by thiostrepton (Fig. 8f). Together, rheumatoid arthritis synovial $CX_3CR1^+HLA\text{-}DR^{hi}CD11c^+CD86^+$ cells have high osteoclastogenic potential, and FoxM1 constitutes a potential target for rheumatoid arthritis treatment.

Discussion

We have provided a detailed assessment of the differentiation trajectory of inflammatory osteoclast precursors, and identified a distinct arthritis-associated macrophage population, AtoM, that is responsible for articular bone erosion in pannus. Although extensive studies have identified monocytoid cells with osteoclastogenic potential in the BM or spleen under various conditions[8–10,13,37], pathogenic osteoclasts formed on the pannus–bone interface are derived from circulating blood monocytes that ingress into the synovium, and a precise analysis of the inflamed synovium is indispensable to identify the in situ osteoclast precursor population in the arthritic condition. Our protocol succeeded in isolating the inflamed synovium on the bare area[11], which can be confirmed by its unique flow cytometric plots compared with those of other organs. We also demonstrated that $CD45^+CX_3CR1^{lo}Ly6C^{hi}$ populations in the blood (R1) and inflamed synovium (R2) have substantially distinct transcriptional profiles in terms of chemokines (*Cxcl1*, *Cxcl2*, *Ccl2*, *Ccl3* and *Ccl4*) and inflammatory cytokines (*Il1*, *Il6* and *Tnf*). Distinguishing synovial cells from BM cells enabled us to identify a unique macrophage population, AtoM, suggesting that macrophage subtypes in vivo should be defined depending on the organs in which they reside and corresponding diseases, rather than the simple terminology of M1 and M2 macrophages.

Notably, AtoMs highly express several cell-surface molecules for antigen presentation, including major histocompatibility complex class II and CD80/86. Despite its controversy, this result may suggest that osteoclasts in arthritic joints derived from AtoMs are involved in antigen presentation in local foci. A previous study of inflammatory bowel disease reported that osteoclasts generated under inflammatory conditions are efficient at inducing TNF-producing $CD4^+$ T cells, amplifying both the inflammatory response and bone destruction[10]. Other studies have also shown that dendritic cells can differentiate into osteoclasts under inflammatory conditions[38,39]. Although the F4/80 expression and structural phenotype of AtoMs (for example, vacuolar cytoplasm) suggest that they can be classified

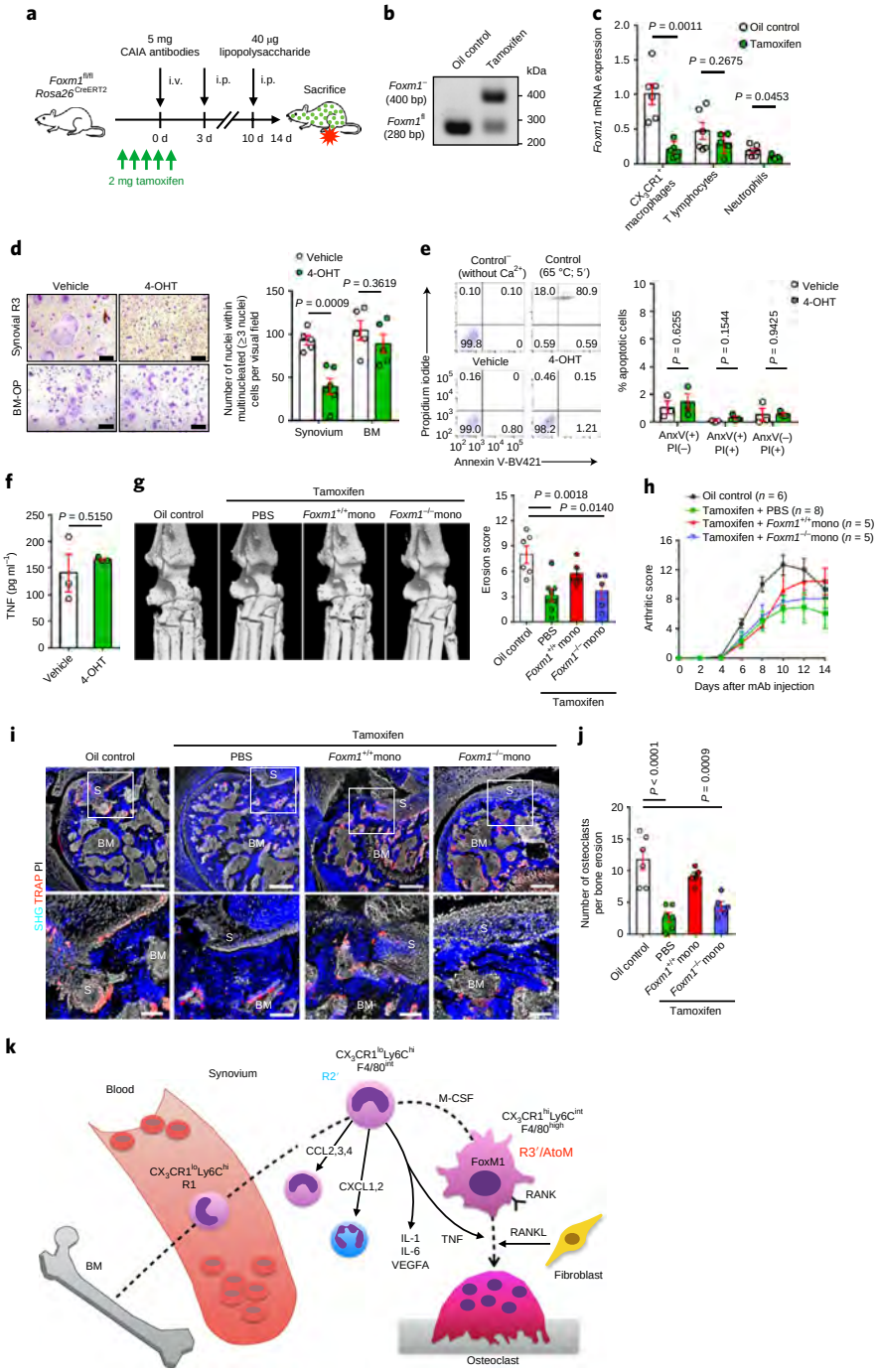

Fig. 7 | FoxM1 contributes to arthritis-induced bone destruction. a, Experimental design schematic for the CAIA model. i.p., intraperitoneally; i.v., intravenously. **b**, Semi-quantitative PCR analysis to detect the deletion of *Foxm1* (*Foxm1*$^{-}$) and the loxP-flanked *Foxm1* allele (*Foxm1*^{fl}) in the genomic DNA of BM cells. The image is representative of three independent experiments with similar results. bp, base pairs. **c**, *Foxm1* RT-PCR analysis in CX_3CR1^+ monocytes/macrophages, T lymphocytes and neutrophils in BM treated with oil control or tamoxifen in vivo ($n = 6$ mice in the vehicle group and $n = 5$ mice in the tamoxifen group). **d**, RANKL-induced osteoclastogenesis of R3 cells from inflamed knee synovium and BM-OPs from control BM, with vehicle or 4 µM 4-OHT. Scale bars: 200 µm ($n = 5$ mice, except for the synovium/4-OHT group ($n = 6$ mice)). **e**, Flow cytometry analysis of annexin-V- (anxV-) and propidium iodide- (PI-) positive synovial R3 cells treated with vehicle or 4 µM 4-OHT for 72 h ($n = 3$ mice per group). **f**, ELISA of TNF in the cell culture supernatant of synovial R3 cells treated with vehicle or 4 µM 4-OHT for 48 h ($n = 3$ mice per group). **g**, Representative 3D reconstructions and erosion scores of rear paws by micro-CT analysis. CAIA mice treated with oil control ($n = 6$ mice), tamoxifen ($n = 8$ mice), or tamoxifen plus adoptive transfer of *Foxm1*$^{+/+}CX_3CR1^+$ cells or *Foxm1*$^{-/-}CX_3CR1^+$ cells ($n = 5$ mice each) were analyzed. **h**, Clinical arthritic scores of CAIA mice. mAb, monoclonal antibody. **i**,**j**, Histological examination of knee joints (**i**) and number of osteoclasts per visual field at the sites of bone erosions (**j**) from CAIA mice treated with oil control, tamoxifen, or tamoxifen plus adoptive transfer of *Foxm1*$^{+/+}CX_3CR1^+$ cells or *Foxm1*$^{-/-}CX_3CR1^+$ cells. Cells were stained with propidium iodide (PI). Values represent the average count of three different sections ($n = 6$ mice for the oil control and tamoxifen + PBS; $n = 5$ mice for tamoxifen + adoptive transfer). Scale bars: 300 µm (top row) and 100 µm (bottom row). **k**, Schematic of the differentiation trajectory of inflammatory osteoclast precursors in arthritis. Statistical significance was determined by unpaired two-tailed *t*-test (**c**–**f**) or one-way ANOVA with Bonferroni's post-hoc test (**g** and **j**). Data represent means ± s.e.m. for each group. Symbols represent individual mice.

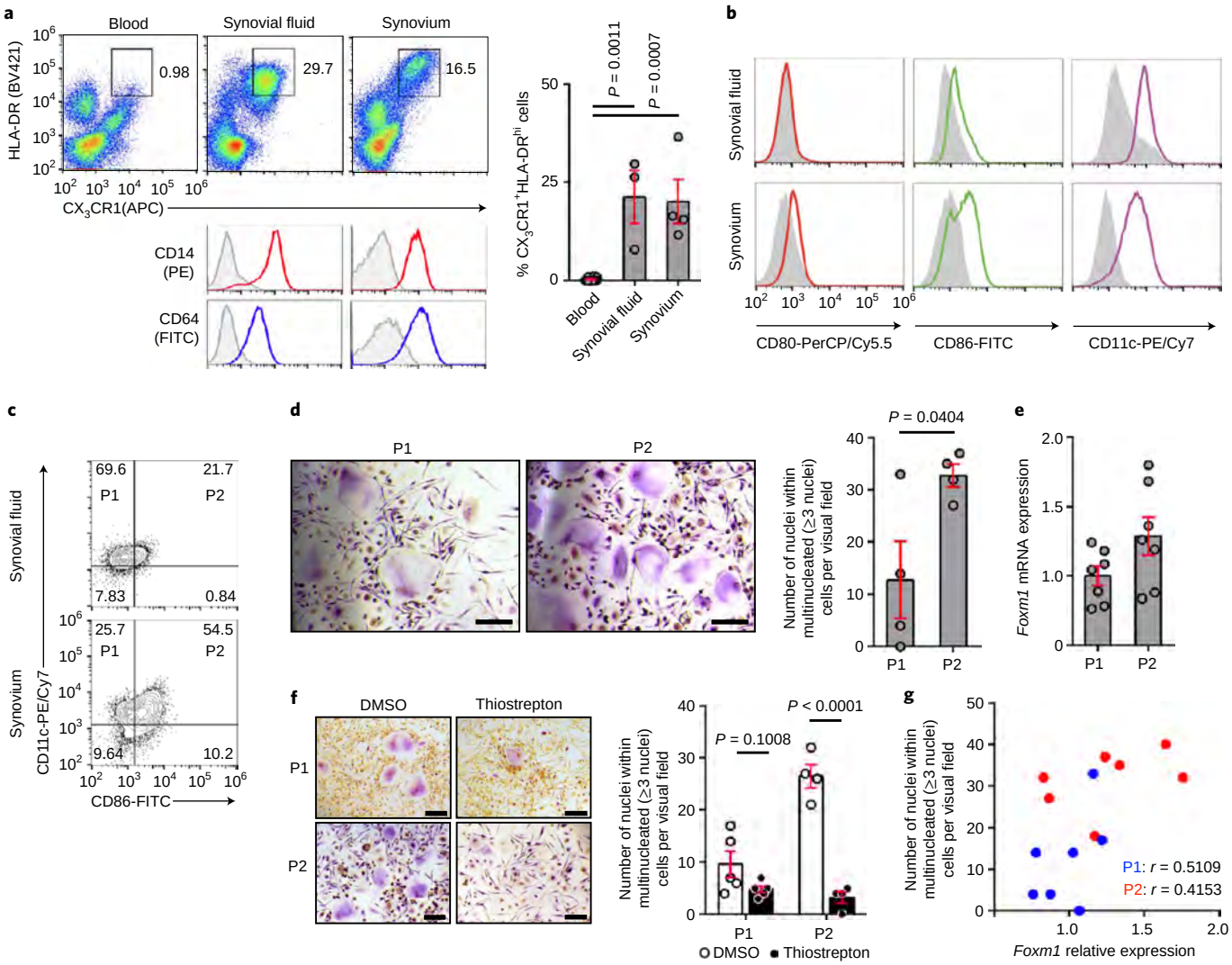

Fig. 8 | Rheumatoid arthritis synovial $CX_3CR1^+HLA\text{-}DR^{hi}CD11c^+CD86^+$ cells have high osteoclastogenic potential. a, Phenotypic characterization of $CD45^+CX_3CR1^+HLA\text{-}DR^+$ cells in the blood, synovial fluid and synovium of patients with rheumatoid arthritis ($n=10$ for blood; $n=3$ for synovial fluid; $n=4$ for synovium). Percentages of cells are relative to $CD45^+$ cells. **b**, Phenotypic characterization with the indicated cell-surface markers on $CX_3CR1^+HLA\text{-}DR^{hi}$ cells of synovial fluid and synovium of patients with rheumatoid arthritis. Shaded regions indicate staining with isotype controls. **c**, Contour plots of $CD45^+CX_3CR1^+HLA\text{-}DR^{hi}$ cells gated by CD11c and CD86. $CD11c^+CD86^-$ cells were termed P1 cells and $CD11c^+CD86^+$ cells were termed P2 cells. Data are representative of at least three independent experiments with similar results. **d**, RANKL-induced osteoclastogenesis of $CX_3CR1^+HLA\text{-}DR^{hi}CD11c^+CD86^-$ cells (P1) and $CX_3CR1^+HLA\text{-}DR^{hi}CD11c^+CD86^+$ cells (P2) from synovial fluid of patients with rheumatoid arthritis. Scale bars: 200 μm ($n=4$ per group). **e**, *Foxm1* RT-PCR analysis of P1 and P2 cells ($n=7$ per group). **f**, RANKL-induced osteoclastogenesis of P1 ($n=5$) and P2 cells ($n=4$) treated with DMSO or 0.5 μM thiostrepton. **g**, Correlation of osteoclastogenic ability and relative *Foxm1* expression in P1 and P2 cells, where *r* is the correlation coefficient ($n=7$ per group). Statistical significance was determined by one-way ANOVA with Bonferroni's post-hoc test (**a**) or unpaired two-tailed *t*-test (**d** and **f**). Data represent means ± s.e.m. for each group. Symbols represent individual human patients.

as macrophages, the expression of dendritic cell markers such as CD11c and major histocompatibility complex class II implies that AtoMs may share functional characteristics with both macrophages and dendritic cells.

FoxM1 plays a prominent role in carcinogenesis by rendering tumor cells more aggressive and invasive[24]; however, it has never been reported in the context of autoimmune diseases. A previous study showed that FoxM1 directly drives mitochondrial biogenesis[40], which is crucial for differentiation into osteoclasts[41], and our RNA-Seq data are consistent with this finding, in that AtoMs were significantly enriched with genes associated with mitochondrial translation and oxidative phosphorylation. Thus, FoxM1 may play a role in AtoMs by meeting the high energy demand for osteoclastogenesis under arthritic conditions. Because global FoxM1 inhibition alleviated not only articular bone destruction but also inflammation, it is possible that other cells outside the myeloid lineage influence the inflammatory process via FoxM1, which can indirectly affect bone destruction. Future studies are needed to advance our knowledge on this subject.

In human cells, several studies have reported that macrophages in the synovial fluid and synovium of patients with rheumatoid arthritis express CX_3CR1 (refs. [42–44]); HLA-DR has also been used to categorize human blood monocytes[16]. Because mouse AtoMs express CX_3CR1 and I-A/I-E, the application of these two markers in samples from patients with rheumatoid arthritis facilitated identification of the $CX_3CR1^+HLA\text{-}DR^{hi}$ population in the synovial samples, and we further revealed that human synovial osteoclast precursors were included in the $CX_3CR1^+HLA\text{-}DR^{hi}CD11c^+CD86^+$

population. An anti-fractalkine monoclonal antibody phase-1/2 clinical trial showed an effective clinical response in active patients with rheumatoid arthritis[45], and further analysis of osteoclastogenesis and chemotactic activity in these cells may improve our understanding of its pathophysiology in rheumatoid arthritis.

Our protocol allows for the precise isolation of inflamed synovium from arthritic mice and may facilitate investigations to determine the role of other immune cells involved in pannus in situ, including lymphocytes, fibroblasts and endothelial cells. In addition, the targeting of FoxM1 is distinct from therapies targeting CX_3CL1 (fractalkine) because CX_3CR1^+ cells do not necessarily depend on the CX_3CL1–CX_3CR1 axis for chemotaxis within the synovial tissue, and chemotaxis is not directly involved in osteoclastogenesis. Furthermore, pathological bone destruction represents a final common pathway in several chronic inflammatory disorders, including histiocytosis, spondyloarthritis and sarcoidosis, which are responsible for substantial disability and morbidity[6]. The identification of arthritis-associated osteoclast precursors implies that the resultant osteoclasts are more heterogeneous than presently thought, and an understanding of the dynamics of pathological osteoclastogenesis should prompt the development of optimized treatment for inflammatory bone destruction.

Online content

Any methods, additional references, Nature Research reporting summaries, source data, extended data, supplementary information, acknowledgements, peer review information; details of author contributions and competing interests; and statements of data and code availability are available at https://doi.org/10.1038/s41590-019-0526-7.

Received: 29 October 2018; Accepted: 24 September 2019;
Published online: 18 November 2019

References

1. Pirzgalska, R. M. et al. Sympathetic neuron-associated macrophages contribute to obesity by importing and metabolizing norepinephrine. *Nat. Med.* **23**, 1309–1318 (2017).
2. Okabe, Y. & Medzhitov, R. Tissue-specific signals control reversible program of localization and functional polarization of macrophages. *Cell* **157**, 832–844 (2014).
3. Satoh, T. et al. Identification of an atypical monocyte and committed progenitor involved in fibrosis. *Nature* **541**, 96–101 (2017).
4. Asano, K. et al. CD169-positive macrophages dominate antitumor immunity by crosspresenting dead cell-associated antigens. *Immunity* **34**, 85–95 (2011).
5. Arai, F. et al. Commitment and differentiation of osteoclast precursor cells by the sequential expression of c-Fms and receptor activator of nuclear factor κB (RANK) receptors. *J. Exp. Med.* **190**, 1741–1754 (2002).
6. Schett, G. & Gravallese, E. Bone erosion in rheumatoid arthritis: mechanisms, diagnosis and treatment. *Nat. Rev. Rheumatol.* **8**, 656–664 (2012).
7. McInnes, I. The pathogenesis of rheumatoid arthritis. *N. Engl. J. Med.* **365**, 2205–2219 (2011).
8. Charles, J. F. et al. Inflammatory arthritis increases mouse osteoclast precursors with myeloid suppressor function. *J. Clin. Invest.* **122**, 4592–4605 (2012).
9. Seeling, M. et al. Inflammatory monocytes and Fc receptor IV on osteoclasts are critical for bone destruction during inflammatory arthritis in mice. *Proc. Natl Acad. Sci. USA* **110**, 10729–10734 (2013).
10. Ibáñez, L. et al. Inflammatory osteoclasts prime TNFα-producing $CD4^+$ T cells and express CX_3CR1. *J. Bone Miner. Res.* **31**, 1899–1908 (2016).
11. Werner, D. et al. Early changes of the cortical micro-channel system in the bare area of the joints of patients with rheumatoid arthritis. *Arthritis Rheumatol.* **69**, 1580–1587 (2017).
12. Adamopoulos, I. E. & Mellins, E. D. Alternative pathways of osteoclastogenesis in inflammatory arthritis. *Nat. Rev. Rheumatol.* **11**, 189–194 (2015).
13. Jacome-Galarza, C. E., Lee, S. K., Lorenzo, J. A. & Aguila, H. L. Identification, characterization, and isolation of a common progenitor for osteoclasts, macrophages, and dendritic cells from murine bone marrow and periphery. *J. Bone Miner. Res.* **28**, 1203–1213 (2013).
14. Ishii, M. et al. Sphingosine-1-phosphate mobilizes osteoclast precursors and regulates bone homeostasis. *Nature* **458**, 524–528 (2009).
15. Misharin, A. V. et al. Non-classical $Ly6C^-$ monocytes drive the development of inflammatory arthritis in mice. *Cell Rep.* **9**, 591–604 (2014).
16. Geissmann, F., Jung, S. & Littman, D. R. Blood monocytes consist of two principal subsets with distinct migratory properties. *Immunity* **19**, 71–82 (2003).
17. Yona, S. et al. Fate mapping reveals origins and dynamics of monocytes and tissue macrophages under homeostasis. *Immunity* **38**, 79–91 (2013).
18. Yokota, K. et al. Combination of tumor necrosis factor α and interleukin-6 induces mouse osteoclast-like cells with bone resorption activity both in vitro and in vivo. *Arthritis Rheumatol.* **66**, 121–129 (2014).
19. O'Brien, W. et al. RANK-independent osteoclast formation and bone erosion in inflammatory arthritis. *Arthritis Rheumatol.* **68**, 2889–2900 (2016).
20. Lam, J. et al. TNF-α induces osteoclastogenesis by direct stimulation of macrophages exposed to permissive levels of RANK ligand. *J. Clin. Invest.* **106**, 1481–1488 (2000).
21. Ochi, S. et al. Pathological role of osteoclast costimulation in arthritis-induced bone loss. *Proc. Natl Acad. Sci. USA* **104**, 11394–11399 (2007).
22. Tamura, T. et al. Soluble interleukin-6 receptor triggers osteoclast formation by interleukin 6. *Proc. Natl Acad. Sci. USA* **90**, 11924–11928 (2006).
23. Murata, K. et al. Hypoxia-sensitive COMMD1 integrates signaling and cellular metabolism in human macrophages and suppresses osteoclastogenesis. *Immunity* **47**, 66–79 (2017).
24. Lam, E. W.-F., Brosens, J. J., Gomes, A. R. & Koo, C.-Y. Forkhead box proteins: tuning forks for transcriptional harmony. *Nat. Rev. Cancer* **13**, 482–495 (2013).
25. Wang, Z., Banerjee, S., Kong, D., Li, Y. & Sarkar, F. H. Down-regulation of forkhead box M1 transcription factor leads to the inhibition of invasion and angiogenesis of pancreatic cancer cells. *Cancer Res.* **67**, 8293–8300 (2007).
26. Hegde, N. S., Sanders, D. A., Rodriguez, R. & Balasubramanian, S. The transcription factor FOXM1 is a cellular target of the natural product thiostrepton. *Nat. Chem.* **3**, 725–731 (2011).
27. Halasi, M. & Gartel, A. L. A novel mode of FoxM1 regulation: positive auto-regulatory loop. *Cell Cycle* **8**, 1966–1967 (2009).
28. Kwok, J. M.-M. et al. Thiostrepton selectively targets breast cancer cells through inhibition of forkhead box M1 expression. *Mol. Cancer Ther.* **7**, 2022–2032 (2008).
29. Mbalaviele, G., Novack, D. V., Schett, G. & Teitelbaum, S. L. Inflammatory osteolysis: a conspiracy against bone. *J. Clin. Invest.* **127**, 2030–2039 (2017).
30. Hasegawa, T., Kaneko, Y., Izumi, K. & Takeuchi, T. Efficacy of denosumab combined with bDMARDs on radiographic progression in rheumatoid arthritis. *Joint Bone Spine* **84**, 379–380 (2017).
31. Campbell, I. K., Rich, M. J., Bischof, R. J. & Hamilton, J. A. The colony-stimulating factors and collagen-induced arthritis: exacerbation of disease by M-CSF and G-CSF and requirement for endogenous M-CSF. *J. Leukoc. Biol.* **68**, 144–150 (2000).
32. Ando, W. et al. Imatinib mesylate inhibits osteoclastogenesis and joint destruction in rats with collagen-induced arthritis (CIA). *J. Bone Miner. Metab.* **24**, 274–282 (2006).
33. Hamilton, J. A. Colony-stimulating factors in inflammation and autoimmunity. *Nat. Rev. Immunol.* **8**, 533–544 (2008).
34. Campbell, I. K., Ianches, G. & Hamilton, J. A. Production of macrophage colony-stimulating factor (M-CSF) by human articular cartilage and chondrocytes. Modulation by interleukin-1 and tumor necrosis factor α. *Biochim. Biophys. Acta* **1182**, 57–63 (1993).
35. Nakano, K. et al. Rheumatoid synovial endothelial cells produce macrophage colony-stimulating factor leading to osteoclastogenesis in rheumatoid arthritis. *Rheumatology* **46**, 597–603 (2007).
36. Hutamekalin, P. et al. Collagen antibody-induced arthritis in mice: development of a new arthritogenic 5-clone cocktail of monoclonal anti-type II collagen antibodies. *J. Immunol. Methods* **343**, 49–55 (2009).
37. Šućur, A. et al. Induction of osteoclast progenitors in inflammatory conditions: key to bone destruction in arthritis. *Int. Orthop.* **38**, 1893–1903 (2014).
38. Wakkach, A. et al. Bone marrow microenvironment controls the in vivo differentiation of murine dendritic cells into osteoclasts. *Blood* **112**, 5074–5083 (2008).
39. Rivollier, A. et al. Immature dendritic cell transdifferentiation into osteoclasts: a novel pathway sustained by the rheumatoid arthritis microenvironment. *Blood* **104**, 4029–4037 (2004).
40. De Luca, A. et al. Mitochondrial biogenesis is required for the anchorage-independent survival and propagation of stem-like cancer cells. *Oncotarget* **6**, 14777–14795 (2015).
41. Ishii, K. A. et al. Coordination of PGC-1β and iron uptake in mitochondrial biogenesis and osteoclast activation. *Nat. Med.* **15**, 259–266 (2009).

42. Ruth, J. H. et al. Fractalkine, a novel chemokine in rheumatoid arthritis and in rat adjuvant-induced arthritis. *Arthritis Rheum.* **44**, 1568–1581 (2001).
43. Blaschke, S. et al. Proinflammatory role of fractalkine (CX_3CL1) in rheumatoid arthritis. *J. Rheumatol.* **30**, 1918–1927 (2003).
44. Nanki, T., Imai, T. & Kawai, S. Fractalkine/CX_3CL1 in rheumatoid arthritis. *Mod. Rheumatol.* **27**, 392–397 (2017).
45. Tanaka, Y. et al. Safety, pharmacokinetics, and efficacy of E6011, an antifractalkine monoclonal antibody, in a first-in-patient phase 1/2 study on rheumatoid arthritis. *Mod. Rheumatol.* **28**, 58–65 (2018).

Methods

Mice. Wild-type DBA/1J mice were obtained from Oriental Yeast in Japan. CX_3CR1-EGFP knock-in mice[46] and TRAP promoter-tdTomato transgenic mice[47] derived from the C57BL/6J (B6) background were backcrossed for more than ten generations onto DBA/1J mice. The *Foxm1 LoxP/LoxP*$^{fl/fl}$ mice were bred with *Rosa26*^{CreERT2} mice by A.H. (Kanazawa University, Japan). Lyz2-Cre transgenic mice were provided by S. Akira (Osaka University, Japan)[48]. All mice were bred and maintained under specific-pathogen-free conditions at the animal facilities of Osaka University, and all animal experiments were performed in accordance with the Osaka University Animal Experimental Guidelines using approved protocols. Mutant mice were genotyped by PCR. To detect the *Foxm1 flox* allele, we used the primers TGGCTTCCCAGCAGTACAAATC and TGCTTACAAAAGACACACTTGGACG. To detect the deleted *Foxm1* allele, we used the primers TGGCTTCCCAGCAGTACAAATC and TCTCGCTCAATTCCAAGACCAG.

Samples from patients with rheumatoid arthritis. Research involving human subjects was approved by the Institutional Review Board of Osaka University, with the appropriate informed consent. All patients with rheumatoid arthritis fulfilled the American College of Rheumatology 2010 Rheumatoid Arthritis classification criteria. Clinical information, including seropositivity and medication usage, was obtained by reviewing electronic medical records (Supplementary Table 2). Synovial tissue specimens were obtained from patients with rheumatoid arthritis undergoing joint replacement surgery or synovectomy at Osaka University Hospital. The tissue was minced and digested with 3 mg ml^{-1} type I collagenase (Worthington) in Hank's Balanced Salt Solution (HBSS), and incubated at 37 °C for 30 min, with inversion every 5 min. Disaggregated tissue elements were passed through a 70-μm cell strainer. Synovial fluid samples were obtained as excess material from patients with rheumatoid arthritis and knee effusion undergoing therapeutic arthrocentesis. Blood samples were obtained from patients with rheumatoid arthritis, and subjected to density centrifugation using Lymphoprep (AXS) to isolate the mononuclear cells.

Induction and evaluation of CIA. Arthritis was induced in DBA/1J mice (Oriental Yeast) between 8 and 10 weeks of age, as described previously[49]. Chicken type II collagen (cCII; Sigma Chemical) was dissolved in 0.05 M acetic acid to a concentration of 4 mg ml^{-1} by overnight rotation at 4 °C, and mixed with an equal volume of Freund's complete adjuvant (2 mg ml^{-1} *Mycobacterium tuberculosis*; Chondrex). On day 0, DBA/1J mice were immunized at the base of the tail with 100 μl emulsion. The same injection was repeated on day 21. The severity of arthritis was evaluated using an established semi-quantitative scoring system with a five-point scale, where 0 = no swelling, 1 = mild swelling confined to the tarsals or ankle joint, 2 = mild swelling extending from the ankle to the tarsals, 3 = moderate swelling extending from the ankle to the metatarsal joints and 4 = severe swelling encompassing the ankle, foot and digits. The cumulative score for the four paws of each mouse (maximum score: 16) was used as the arthritis score to represent overall disease severity, as described previously[49].

Induction and evaluation of CAIA. Arthritis was induced by injecting 5 mg 5-clone Arthrogen-CAIA antibody (Chondrex) intravenously on day 0, and 40 μg lipopolysaccharide intraperitoneally on days 3 and 10. Mice were evaluated on day 14. The severity of arthritis was evaluated with the same semi-quantitative method used for the CIA model.

For *Foxm1*$^{+/+}$ monocyte adoptive transfer, $CX_3CR1^+Ly6C^{hi}$ monocytes from wild-type mice were sorted using an SH800 cell sorter (Sony). For *Foxm1*$^{-/-}$ monocyte adoptive transfer, $CX_3CR1^+Ly6C^{hi}$ monocytes from *Foxm1*$^{fl/fl}$*Rosa26*^{CreERT2} mice treated with 2 mg tamoxifen for 5 d were sorted. Aliquots of 1×10^6 cells per mouse were administered intravenously to the tamoxifen-treated mice intravenously on days 1, 6 and 12.

Induction of DSS colitis. To induce acute colitis, mice received 2% DSS salt (Wako) ad libitum in sterile drinking water. Mice were then sacrificed on day 6.

Parabiosis. Male 8-week-old double-transgenic mice (CX_3CR1-EGFP/TRAP-tdTomato) were surgically connected to wild-type mice as described previously[50]. The mice were anesthetized with isoflurane. The lateral aspects of each mouse were shaved and treated with hair-removal lotion (Epilat; Kracie). After corresponding lateral skin incisions were made from the elbow to the knee in each mouse, the forelimbs and hind limbs were tied together using silk sutures. Incisions of approximately 1 cm were made in the peritoneum of each mouse, and the mice were attached using silk sutures. The skin incisions were closed using stainless steel wound clips. To ensure the animals' wellbeing for 8 weeks, individual parabiotic mouse pairs were placed in clean cages, and food pellets were broken into pieces, soaked in water and placed on the floor to minimize the strain of reaching for food. Shared blood circulation was confirmed by the presence of EGFP$^+$ cells in the peripheral blood of wild-type parabionts.

BM transplantation. Recipient mice were administered a single 10-Gy dose of whole-body irradiation. After 6 h, 3 million unfractionated BM cells from donor mice were injected intravenously. Bone marrow reconstitution was confirmed by immunohistological analysis of tdTomato and EGFP$^+$ cells in the BM at the observation endpoint.

Isolation of leukocytes from tissues. Tissues were harvested and prepared as follows. After sacrifice under anesthesia, the right auricles of the mice were cut and 15 ml of pre-warmed 1× phosphate buffered saline (PBS) was injected into the left ventricle for perfusion. Perfusion was omitted in the experiments designed to assess blood samples.

Because knee joints are covered with muscles, direct macroscopic observation of arthritis is challenging. Therefore, we selected mice with arthritic paws, and confirmed substantial inflammation in knee joints by direct exposure of the inflamed synovium using the following protocol. Mice were perfused with 15 ml pre-warmed 1× PBS. After removal of the skin and biceps femoris muscle, the quadriceps femoris muscles including the vastus intermedius muscle were pinched and lifted with tweezers. The quadriceps femoris muscles and patellar ligament, including the patella, were removed from the knee joint under a stereoscopic microscope (SMZ 745T; Nikon). The hypertrophied synovium was isolated without damaging the bone (Supplementary Fig. 1b). Ankle joint tendons, including the Achilles tendon, were removed, revealing the hypertrophied synovium around the talus, which allowed for isolation without damaging the bone (Supplementary Fig. 1d). Synovial tissues were digested with 3 mg ml^{-1} type I collagenase in HBSS, and incubated at 37 °C for 30 min. Disaggregated tissue elements were passed through a 70-μm cell strainer.

The BM, spleen and liver were minced and passed through a 70-μm cell strainer. The kidney, lung and brain were harvested, minced and digested for 30 min in RPMI containing 1 mg ml^{-1} type I collagenase (Worthington) and 5% heat-inactivated fetal bovine serum at 37 °C, to obtain single-cell suspensions. For isolation of colonic lamina propria cells, the entire colon was cut longitudinally and washed to remove all of the excess fat and feces. The tissues were then incubated in calcium/magnesium-free HBSS containing 5 mM EDTA at 37 °C for 20 min on a shaking incubator. After removal of the epithelial cells, the tissues were finely minced and incubated in RPMI containing 1 mg ml^{-1} type IV collagenase, 600 U ml^{-1} DNase IV (Qiagen), 0.5 mg ml^{-1} Dispase (Invitrogen) and 5% fetal bovine serum for 50 min at 37 °C in a shaking incubator. The resulting cell suspension was passed through a 70-μm cell strainer and centrifuged at 1,500 r.p.m. for 5 min to prepare for flow cytometry analysis.

Flow cytometry. Measurements were performed on an SH800 cell sorter (Sony) and analyzed with FlowJo software (Tree Star). Isolated murine cells were blocked with anti-CD16/32 antibody (553141; BD Biosciences; 2.4G2; 8330543) for 10 min, followed by staining with the following antibodies for 15 min: anti-CD45-PB (103126; BioLegend; 30-F11; B253970), anti-CD80-PB (104724; BioLegend; 16-10A1; B177884), anti-CD86-PB (105021; BioLegend; GL-1), anti-CD3-BV421 (100227; BioLegend; 17A2; B245756), anti-Ly6G-BV421 (127627; BioLegend; 1A8; B241491), Streptavidin-BV421 (405226; BioLegend; B274676), anti-F4/80-BV421 (123137; BioLegend; BM8; B226240), anti-I-A/I-E-Biotin (107603; BioLegend; M5/114.15.2; B189443), anti-CD11c-Biotin (117304; BioLegend; N418; B270359), anti-CD265 (RANK)-Biotin (13-6612-81; eBioscience; R12-31; E03168-1632), Lineage Cell Detection Cocktail-Biotin (130-092-613; Miltenyi Biotec; 5161024423), anti-CD3-PE (100308; BioLegend; 145-2C11; B234582), anti-CD140a-PE (135905; BioLegend; APA5; B244566), Streptavidin-PE (405203; BioLegend; B245809), anti-CD45-FITC (103108; BioLegend; 30-F11; B176444), anti-CX_3CR1-FITC (149019; BioLegend; SA011F11; B233462), anti-Ly6C-APC (560595; BD Biosciences; AL-21; 7082897), anti-CX_3CR1-APC (149007; BioLegend; SA011F11; B258626), anti-CD45-PE/Cy7 (103114; BioLegend; 30-F11; B271123), anti-CD31-AF647 (102516; BioLegend; MEC13.3; B245809), anti-CCR2-PE/Cy7 (150611; BioLegend; SA203G11; B227440), Biotin-Rat IgG2a,κ isotype control (400503; BioLegend; RTK2758; B227705), PB-Rat IgG2a,κ isotype control (400527; BioLegend; RTK2758; B135167), PB-Armenian Hamster IgG isotype control (400925; BioLegend; HTK888; B133580), BV421-Armenian Hamster IgG isotype control (400935; BioLegend; HTK888; B266305) and PE/Cy7-Rat IgG2a,κ isotype control (400521; BioLegend; RTK2758; B236195).

The following antibodies were used for human samples: anti-HLA-DR-BV421 (307635; BioLegend; L243; B223586), anti-CD64-FITC (305005; BioLegend; 10.1; B216437), anti-CD86-FITC (374203; BioLegend; BU63; B274424), anti-CD14-PE (325605; BioLegend; HCD14; B188762), anti-CX_3CR1-APC (341609; BioLegend; 2A9-1; B219658), anti-CD80-PerCP/Cy5.5 (305231; BioLegend; 2D10; B236173), anti-CD45-PE/Cy7 (304015; BioLegend; H130; B229088), anti-CD11c-PE/Cy7 (561356; BD Biosciences; B-ly6; 5114612) and Fc Receptor Blocking Solution (422301; BioLegend; B215860).

For intracellular staining, 200 μl fixation/permeabilization working solution (00-5523-00; eBioscience) was added to each sample, and the mixtures were incubated for 60 min at room temperature. After blockade with anti-CD16/32 antibody, FoxM1 antibody (175798; Abcam; GR316488-1) in 100 μl permeabilization buffer (00-5523-00; eBioscience) was added to each sample. Samples were subsequently washed and stained with anti-rabbit biotinylated antibody (BA-1000; Vector; W2206) and Streptavidin-PE.

Histology and immunohistochemistry. Mice were euthanized at various time points, and tissues were fixed by perfusion with 4% paraformaldehyde. Dissected knee joints were further fixed with 4% paraformaldehyde for 3 h at 4 °C. The samples were frozen in chilled hexane (Wako) using dry ice, and 12-μm-thick sections of non-decalcified knee joints were prepared using a Multi-Purpose Cryosection Preparation Kit[51] (Section Lab and Leica Microsystems). A standard protocol was used for hematoxylin and eosin staining, and immunohistological analyses were performed as described previously[14]. Fluorescence-based staining for TRAP with ELF97 substrate (Life Technologies) was used with some modifications. Anti-M-CSF antibody (sc-365779; Santa Cruz Biotechnology; D4; B2417) was biotinylated in our laboratory using a Biotin Labeling Kit-NH_2 (Dojindo Molecular Technologies). Samples were stained with anti-M-CSF biotinylated antibody, followed by staining with Streptavidin-FITC (405201; BioLegend; B190907) for 60 min at room temperature. Samples were observed using a TCS-SP5 confocal microscope (Leica Microsystems) and illuminated with a laser (wavelengths: 405 nm for ELF97 and BV421; 488 nm for EGFP; and 561 nm for propidium iodide and tdTomato). Collagen-enriched bone matrices and synovial fibrous tissues were visualized using the SHG with the infrared lasers of a TCS-SP5 multi-photon laser microscope (wavelength 880 nm) driven by a Chameleon XR Sapphire laser (Coherent), which also excites EGFP. Emission signals were obtained by setting the wavelength to 420–470 nm for BV421, 500–550 nm for ELF97, EGFP and fluorescein isothiocyanate, 580–630 nm for tdTomato, 600–630 nm for propidium iodide, and 430–480 nm for SHG. For cell counting of healthy synovium, synovial fibers and bones were identified with SHG, and three knee joint sections per mouse were analyzed using Imaris software (Bitplane) (Supplementary Fig. 2a). Knee joints were used for histological examination because articular anatomical structures, such as the synovium and bare area, were easily discerned microscopically in both inflamed and uninflamed conditions, unlike paws, where small tarsal bones tightly adhere to each other.

Reverse-transcription PCR (RT-PCR) analyses. Total RNA and complementary DNA of the cells from each tissue were obtained with an RNeasy Mini Kit (Qiagen) and Superscript III reverse transcriptase (Thermo Fisher Scientific), according to the manufacturers' instructions. Quantitative RT-PCR was performed for 40 cycles using a Thermal Cycler Dice Real Time System TP800 (Takara). The reactions were normalized relative to the housekeeping gene *β-actin*, and the specificity of the amplified products was confirmed by dissociation curves. The following specific primer pairs were used (forward and reverse, respectively): mouse *β-actin* (5′-TCCTCCCTGGAGAAGAGCTA-3′ and 5′-ATCTCCTTCTGCATCCTGTC-3′); mouse *Foxm1* (5′-GTCTCCTTCTGGACCATTCACC-3′ and 5′-GCTCAGGATTGGGTCGTTTCTG-3′); mouse *csf1* (5′-CCCATATTGCGACACCGAA-3′ and 5′-AAGCAGTAACTGAGCAACGGG-3′); mouse *Rankl* (5′-CAGCATCGCTCTGTTCCTGTA-3′ and 5′-CTGCGTTTTCATGGAGTCTCA-3′); mouse *Tnf* (5′-GCCACCACGCTCTTCTGTCTAC-3′ and 5′-GGGTCTGGGCCATAGAACTGAT-3′); mouse *Il6* (5′-CACATGTTCTCTGGGAAATCG-3′ and 5′-TTGTATCTCTGGAAGTTTCAGATTGTT-3′); mouse *Il1β* (5′-CTGCAGCTGGAGAGTGTGGAT-3′ and 5′-CTCCACTTTGCTCTTGACTTCTATCTT-3′); human *β-actin* (5′-GCGCGGCTACAGCTTCA-3′ and 5′-TGGCCGTCAGGCAGCTCGTA-3′); and human *Foxm1* (5′-CGTCGGCCACTGATTCTCAAA-3′ and 5′-GGCAGGGGATCTCTTAGGTTC-3′).

RNA-Seq. R1, R2′ and R3′ cells from three mice were isolated using an SH800 cell sorter (Sony), and total RNA was extracted using QIAzol lysis reagent (Qiagen), according to the manufacturer's instructions. Sequencing was performed on an Illumina HiSeq 2500 platform in 75-base single-end mode with Illumina Casava 1.8.2 software used for base calling. Sequenced reads were mapped to the mouse reference genome sequences (mm10) using TopHat version 2.0.13 in combination with Bowtie 2 version 2.2.3 and SAMtools version 0.1.19. Fragments per kilobase of exon per million mapped fragments (FPKM) were calculated using Cuffkinks version 2.2.1. The Subio Platform and Subio Basic Plug-in (version 1.20; Subio) were used to calculate the between-sample fold-change analyzed by two-tailed Student's *t*-test ($P<0.1$). Bioinformatics analyses were performed with Ingenuity Pathway Analysis software (Ingenuity Systems; Qiagen). The FPKM score was calculated based on the number of transcribed fragments, and functional associations were computed using the GSEA software (Broad Institute; http://software.broadinstitute.org/gsea/index.jsp). Gene sets from the Broad Institute Molecular Signatures Database and a modified gene set (Supplementary Table 1) were used.

Upstream Regulator Analysis in QIAGEN's Ingenuity Pathway Analysis (Qiagen) was performed to predict the activation or inhibition of transcription factors based on the observed gene expression changes in the gene datasets and the direction of expression changes in R2′ versus R3′ cells. Statistical analysis of the predictions was calculated by the activation *z* score, which can infer the activation states of predicted regulators based on a significant pattern match of up/down-regulation. The strongest predicted activation corresponds to z scores ≥ 2, and the strongest predicted inhibition corresponds to z scores ≤ -2.

Single-cell RNA-Seq analysis. R3 cells were isolated from the inflamed knee synovium of mice with CIA 1 week after arthritis onset. Then, targeted single-cell RNA-Seq analysis was conducted using the BD Rhapsody Single-Cell Analysis System (BD Biosciences), following the manufacture's protocol. In short, the single-cell suspension was loaded into a BD Rhapsody cartridge with >200,000 microwells, and single-cell capture was achieved by random distribution and gravity precipitation. Next, the bead library was loaded into the microwell cartridge to saturation, to promote the pairing of each cell with a bead. The cells were lysed in the microwell cartridge to hybridize mRNA molecules to barcoded capture oligos on the beads. Then, beads were collected from the microwell cartridge into a single tube for subsequent complementary DNA synthesis, *Exo*I digestion and multiplex-PCR-based library construction. For the library construction, we used the customized BD Rhapsody Immune Response Panel for mouse (BD Biosciences), consisting of primer sets for 404 genes. Sequencing was performed on an Illumina HiSeq 3000 platform. The BD Rhapsody Analysis Pipeline was used to process the sequencing data (fastq files), and output result files were analyzed and visualized using the BD DataView software (BD Biosciences). Raw reads from these samples were submitted to the National Center for Biotechnology Information Gene Expression Omnibus database (accession number: GSM3712154).

Micro-computed tomography (micro-CT) of bone tissues. With regard to bone erosion, arthritic hind limbs were scanned with micro-CT (ScanXmate-RX; Comscantechno), and three-dimensional (3D) microstructure images were generated using TRI/3D-Bon software (RATOC Systems). The severity of periarticular erosions was determined by two blinded observers (T.H. and J.K.) using a semi-quantitative method with modifications from a previous report[19]. Six sites in the ankle joint were scored: the talus, navicular bone and medial cuneiform bone, and the bases of the first, second and third metatarsals (Supplementary Fig. 7j). Each site was scored on a scale of 0–3 (0 = normal; 1 = pitting; 2 = full-thickness holes in small–medium areas; and 3 = full-thickness holes in medium–large areas) with a maximum score of 18. The scores of the arthritic hind paw determined by the two observers were averaged to obtain the final erosion score. We used ankles for micro-CT analysis because official radiographic quantification of bone erosion in human patients with rheumatoid arthritis is done in wrists or ankles (Sharp score).

Trabecular bone morphometry within the metaphyseal region of the distal femur was quantified using micro-CT. 3D microstructure images were generated, and bone analysis was performed using TRI/3D-Bon software (RATOC Systems), as described previously[52].

Western blot analysis. Whole-cell protein extracts of inflamed synovium and BM were prepared using radioimmunoprecipitation assay buffer (1× PBS, 0.1% sodium dodecyl sulfate, 1% NP40 and 0.5% sodium deoxycholate) supplemented with protease inhibitors (Sigma–Aldrich), and centrifuged at 4 °C for 10 min at 14,000*g*. The protein concentration was determined by BCA protein assay (Thermo Fisher Scientific). Equal amounts of protein were subjected to electrophoresis on 4–15% gradient sodium dodecyl sulfate-polyacrylamide gels (Bio-Rad) and transferred to PVDF membranes. After blocking with PVDF blocking reagent (Toyobo), the membranes were incubated with primary antibodies in Immunoreaction Enhancer Solution 1 (Toyobo) for 1 h at room temperature, followed by incubation with secondary antibody in Immunoreaction Enhancer Solution 2 (Toyobo) for 1 h at room temperature. Anti-β-actin antibody (20272; Abcam; 1:1,000) and anti-M-CSF antibody (sc-365779; Santa Cruz Biotechnology; 1:1,000) were used.

Analysis of TNF in cell culture supernatants. CAIA was induced in *Foxm1*$^{fl/fl}$*Rosa26*^{CreERT2} mice, and 1×10^4 R3 cells from the inflamed synovium of knee and ankle joints were sorted using an SH800 cell sorter (Sony). After 48 h of incubation with EtOH or 4 μM 4-hydroxytamoxifen (4-OHT), culture medium was replaced and incubated for 24 h with 10 ng ml^{-1} M-CSF in minimal essential medium (MEM). The TNF concentration in the cell culture supernatant was determined by the enzyme-linked immunosorbent assay (ELISA), using the Mouse TNF-alpha ELISA Kit (ab100747; Abcam), based on the manufacturer's protocol.

Treatment with thiostrepton in vivo. Mice with CIA were divided into three treatment groups: vehicle (20% *N*,*N*-dimethylacetamide, 75% polyethylene glycol 400 and 5% Tween 80), low-dose thiostrepton and high-dose thiostrepton. Thiostrepton was injected intraperitoneally at a dose of 20 mg kg^{-1} (low dose) or 50 mg kg^{-1} (high dose) every other day for 3 weeks before sacrifice. For RT-PCR analyses of the inflamed synovium, mice with CIA were sacrificed 2 weeks after starting treatment with vehicle or 50 mg kg^{-1} thiostrepton injection every other day.

For the physiological bone remodeling analyses, male mice were divided into vehicle- and 50 mg/kg thiostrepton-treated groups. Vehicle or thiostrepton was injected intraperitoneally twice a week from 5 weeks of age, and mice were sacrificed at 10 weeks of age.

In vitro osteoclast differentiation. For murine samples, flow cytometry-sorted primary blood monocytes and synovial monocytes/macrophages (1×10^4 cells per sample) were cultured with 10 ng ml^{-1} M-CSF in MEM containing 10% fetal calf serum. After 2 d, cells were cultured for 3 d in MEM containing 10 ng ml^{-1} M-CSF and 100 ng ml^{-1} RANKL, unless otherwise noted. Murine TNF (315-01A; PeproTech), murine IL-6 (406-ML; R&D Systems) and murine OPG (459-MO; R&D Systems) were added at the concentrations indicated in the figure captions and legends. Nunclon Sphera plates (174927; Thermo Fisher Scientific) were used for non-adherent conditions. BM-OPs represent the CD45$^+$CX$_3$CR1$^+$Ly6C^{hi} BM population with osteoclast precursor activity[8,13].

For human samples, flow cytometry-sorted cells (2×10^4 cells per samples) were cultured with 30 ng ml^{-1} M-CSF in MEM containing 10% fetal calf serum for 2 d, followed by incubation with 30 ng ml^{-1} M-CSF and 100 ng ml^{-1} RANKL for 9 d.

Sorting of mature osteoclasts from RepCell. To avoid cell damage during isolation of osteoclasts from plates, the temperature-responsive cell cultureware RepCell (CellSeed) was used. Multiple mice with CIA were sacrificed to isolate 1×10^5 R3 cells from inflamed knee and ankle joints. Sorted R3 cells were incubated with 10 ng ml^{-1} M-CSF for 48 h, followed by incubation with 10 ng ml^{-1} M-CSF and 100 ng ml^{-1} RANKL for 96 h to induce osteoclastogenesis. Cells were gently collected after a 10-min incubation at 4 °C and stained with Hoechst 33342 (1:1,000). The multinucleated FSC^{hi}SSC^{hi} cell population was gated and sorted by flow cytometry.

Bone resorption assay. Primary blood monocytes, synovial macrophages and BM-OPs were isolated from mice with CIA, sorted onto Osteo Assay Surface plates (Corning) coated with inorganic crystalline calcium phosphate, and cultured with 100 ng ml^{-1} RANKL and 10 ng ml^{-1} M-CSF for 6 d. After removing cells with sodium hypochlorite, resorption pits were photographed and analyzed using a BZ-X700 fluorescence microscope (Keyence).

Electroporation. BMMs were obtained from wild-type mice by culturing BM cells collected from the tibias and femurs of 8- to 10-week-old males. Pelleted cells (1×10^6 cells per sample) were suspended in 100 µl Mouse Macrophage Nucleofector Solution (Lonza; VPA-1009), and we combined the cell suspension with cytomegalovirus promoter-driven T7-tagged Foxm1 plasmid (CMV-T7-Foxm1; a gift from P. Raychaudhuri) or mock plasmid. The cell/DNA suspension was transferred into an Amaxa electrode cuvette and electroporated in an Amaxa Nucleofector Device II using program Y-001. Then, the cells were cultured in MEM supplemented with 10 ng ml^{-1} M-CSF for 48 h for RT-PCR analyses.

Statistical analysis. The results are shown as single data points in dot plots, and data represent means ± s.e.m. Between-group differences were determined by two-tailed *t*-test. One-way analysis of variance (ANOVA) with Bonferroni's post-hoc test was used for comparisons among three or more groups. The Kolmogorov–Smirnov test was used for GSEA. Fisher's exact test was used for Ingenuity Pathway Analysis upstream analysis. Associations were assessed using Pearson's correlation. Statistical analyses were performed using GraphPad Prism 6 (GraphPad Software). Animal and human sample sizes are indicated on the dot plots.

Reporting Summary. Further information on research design is available in the Nature Research Reporting Summary linked to this article.

Data availability

The datasets analyzed during the current study are available from the corresponding author on reasonable request. Raw RNA-Seq data and single-cell RNA-Seq data related to this study are available from the Gene Expression Omnibus (accession numbers GSE117149 and GSM3712154, respectively).

References

46. Jung, S. et al. Analysis of fractalkine receptor CX$_3$CR1 function by targeted deletion and green fluorescent protein reporter gene insertion. *Mol. Cell. Biol.* **20**, 4106–4114 (2000).
47. Kikuta, J. et al. Dynamic visualization of RANKL and Th17-mediated osteoclast function. *J. Clin. Invest.* **123**, 866–873 (2013).
48. Takeda, K. et al. Enhanced Th1 activity and development of chronic enterocolitis in mice devoid of Stat3 in macrophages and neutrophils. *Immunity* **10**, 39–49 (1999).
49. Brand, D. D., Latham, K. A. & Rosloniec, E. F. Collagen-induced arthritis. *Nat. Protoc.* **2**, 1269–1275 (2007).
50. Kamran, P. et al. Parabiosis in mice: a detailed protocol. *J. Vis. Exp.* **6**, e50556 (2013).
51. Kawamoto, T. Use of a new adhesive film for the preparation of multi-purpose fresh-frozen sections from hard tissues, whole-animals, insects and plants. *Arch. Histol. Cytol.* **66**, 123–143 (2003).
52. Ishii, M., Kikuta, J., Shimazu, Y., Meier-Schellersheim, M. & Germain, R. N. Chemorepulsion by blood S1P regulates osteoclast precursor mobilization and bone remodeling in vivo. *J. Exp. Med.* **207**, 2793–2798 (2010).

Acknowledgements

We thank R. N. Germain (NIAID/NIH, USA) for critically reviewing this manuscript. This work was supported by CREST at the Japan Science and Technology Agency (J170701506 to M. I.), Grants-in-Aid for Scientific Research (S) from the Japan Society for the Promotion of Science (19H056570 to M.I.), a Grant-in-Aid for Young Scientists (A) from the Japan Society for the Promotion of Science (15H056710 to J.K.), and grants from the Uehara Memorial Foundation (to M.I.), Kanae Foundation for the Promotion of Medical Sciences (to M.I.), Mochida Memorial Foundation (to M.I.), Takeda Science Foundation (to M.I.) and PRIME at the Japan Agency for Medical Research and Development (19gm6210005h to J.K.).

Author contributions

T.H. and M.I. conceived the study. T.H. and J.K. designed the experiments. T.S., Y.M., S.S., T.M., K.Y. and T.T. discussed the experiments and results. K.E. and M.H. provided the samples from patients with rheumatoid arthritis. Y.Y., A.H. and V.V.K. provided the *Foxm1*$^{fl/fl}$ mouse line. A.H. provided the RosaERT2Cre mouse line. D.O. performed the RNA-Seq analysis and single-cell RNA-Seq analysis. T.H. wrote the initial draft. J.K. and M.I. revised the final draft.

Competing interests

The authors declare no competing interests.

Additional information

Supplementary information is available for this paper at https://doi.org/10.1038/s41590-019-0526-7.

Correspondence and requests for materials should be addressed to M.I.

Peer review information Zoltan Fehervari was the primary editor on this article and managed its editorial process and peer review in collaboration with the rest of the editorial team.

Reprints and permissions information is available at www.nature.com/reprints.

nature research

Corresponding author(s): Masaru Ishii

Last updated by author(s): Sep 19, 2019

Reporting Summary

Nature Research wishes to improve the reproducibility of the work that we publish. This form provides structure for consistency and transparency in reporting. For further information on Nature Research policies, see Authors & Referees and the Editorial Policy Checklist.

Statistics

For all statistical analyses, confirm that the following items are present in the figure legend, table legend, main text, or Methods section.

n/a	Confirmed	
☐	☒	The exact sample size (*n*) for each experimental group/condition, given as a discrete number and unit of measurement
☐	☒	A statement on whether measurements were taken from distinct samples or whether the same sample was measured repeatedly
☐	☒	The statistical test(s) used AND whether they are one- or two-sided *Only common tests should be described solely by name; describe more complex techniques in the Methods section.*
☐	☒	A description of all covariates tested
☐	☒	A description of any assumptions or corrections, such as tests of normality and adjustment for multiple comparisons
☐	☒	A full description of the statistical parameters including central tendency (e.g. means) or other basic estimates (e.g. regression coefficient) AND variation (e.g. standard deviation) or associated estimates of uncertainty (e.g. confidence intervals)
☐	☒	For null hypothesis testing, the test statistic (e.g. *F*, *t*, *r*) with confidence intervals, effect sizes, degrees of freedom and *P* value noted *Give P values as exact values whenever suitable.*
☒	☐	For Bayesian analysis, information on the choice of priors and Markov chain Monte Carlo settings
☒	☐	For hierarchical and complex designs, identification of the appropriate level for tests and full reporting of outcomes
☐	☒	Estimates of effect sizes (e.g. Cohen's *d*, Pearson's *r*), indicating how they were calculated

Our web collection on statistics for biologists contains articles on many of the points above.

Software and code

Policy information about availability of computer code

Data collection	RNAseq data were processed by Illumina HiSeq 2500 platform in 75-base single-end mode. Illumina Casava 1.8.2 software was used for base-calling Fluorescent images were collected by Leica SPS. SH800{Sony) was used for FACS and cell sorting. Micro-CT images were generated with TRI/3D-BON software (Ratoc Systems).
Data analysis	TopHat v2.0.13, Bowtie2 ver. 2.2.3, SAMtools ver. 0.1.19, Cuffkinks version 2.2.1, Illumina Casava 1.8.2 software, Subio Platform and Subio Basic Plug-in v1.20, and GSEA software v4.0.1 were used in RNA-sequencing analysis. Flowjo ver.10 was used for FACS data. Fluorescent images were analysed by Imaris software ver.7.5.2 and ver.9.1.2 (Bitplane). RNAseq data were analyzed with Ingenuity Pathway Analysis software (IPA Spring 2017) tSNE plots of single cell RNA-seq analysis was performed by BD Data View software ver.1.2.2. Resorption pits were analyzed using BZ-X analyzer ver.1.4.0.1 (Keyence). Statistics and plots were generated by GraphPad Prism ver.6.

For manuscripts utilizing custom algorithms or software that are central to the research but not yet described in published literature, software must be made available to editors/reviewers. We strongly encourage code deposition in a community repository (e.g. GitHub). See the Nature Research guidelines for submitting code & software for further information.

Data

Policy information about availability of data

All manuscripts must include a data availability statement. This statement should provide the following information, where applicable:

- Accession codes, unique identifiers, or web links for publicly available datasets
- A list of figures that have associated raw data
- A description of any restrictions on data availability

Access to raw RNA-seq data concerning this study is provided through the Gene Expression Omnibus (GEO) (accession number: GSE 117149).
Raw reads of single cell RNA-seq analysis have been submitted to the Gene Expression Omnibus database of National Center for Biotechnology Information (accession no. GSM3712154).
Raw western blot and PCR data are provided in the source data.

Field-specific reporting

Please select the one below that is the best fit for your research. If you are not sure, read the appropriate sections before making your selection.

☒ Life sciences ☐ Behavioural & social sciences ☐ Ecological, evolutionary & environmental sciences

For a reference copy of the document with all sections, see nature.com/documents/nr-reporting-summary-flat.pdf

Life sciences study design

All studies must disclose on these points even when the disclosure is negative.

Sample size	Previously published results, complexity and cost of the experiments, and past experience were used to determine the sample size. For human samples, sample size was determined by the availability of samples. The exact numbers of animal and human samples are indicated on scatter dot plots in each figure.
Data exclusions	There was no data exclusion.
Replication	Experiments included sufficient sample size to ensure the reproducibility of the findings. Representative data was confirmed at least once with an independent experiment. All attempts at replication were successful.
Randomization	The animal were randomly assigned to each experimental/vehicle group.
Blinding	Investigators were blinded to assess the erosion score of CIA and CAIA mice as described in the Method section.

Reporting for specific materials, systems and methods

We require information from authors about some types of materials, experimental systems and methods used in many studies. Here, indicate whether each material, system or method listed is relevant to your study. If you are not sure if a list item applies to your research, read the appropriate section before selecting a response.

Materials & experimental systems

n/a	Involved in the study
☐	☒ Antibodies
☒	☐ Eukaryotic cell lines
☒	☐ Palaeontology
☐	☒ Animals and other organisms
☐	☒ Human research participants
☒	☐ Clinical data

Methods

n/a	Involved in the study
☒	☐ ChIP-seq
☐	☒ Flow cytometry
☒	☐ MRI-based neuroimaging

Antibodies

Antibodies used	For mouse samples: anti-CD16/32 antibody (553141; BD Biosciences; 2.4G2; 8330543), anti-CD45-PB (103126; BioLegend; 30-F11; B253970), anti-CD80-PB (104724; BioLegend; 16-10A1; B177884), anti-CD3-BV421 (100227; BioLegend; 17A2; B245756), anti-Ly6G-BV421 (127627; BioLegend; 1A8; B241491), Streptavidin-BV421 (405226; BioLegend; B274676), anti-F4/80-BV421 (123137; BioLegend; BM8; B226240), anti-I-A/I-E-Biotin (107603; BioLegend; M5/114.15.2; B189443), anti-CD11c-Biotin (117304; BioLegend; N418; B270359), anti-CD265 (RANK)-Biotin (13-6612-81; eBioscience; R12-31; E03168-1632), Lineage cell detection cocktail-Biotin (130-092-613; Miltenyi Biotec; 5161024423), anti-CD3-PE (100308; BioLegend; 145-2C11; B234582), anti-CD140a-PE (135905; BioLegend; APA5; B244566), anti-CD45-FITC (103108; BioLegend; 30-F11; B176444), anti-CX3CR1-FITC (149019; BioLegend; SA011F11; B233462), anti-Ly6C-APC (560595; BD Biosciences; AL-21; 7082897), anti-CX3CR1-APC (149007; BioLegend; SA011F11; B258626), anti-CD45-PE/Cy7 (103114; BioLegend; 30-F11; B271123), anti-CCR2-PE/Cy7 (150611;

BioLegend; SA203G11; B227440), anti-M-CSF (sc-365779; Santa Cruz Biotechnology; D4; B2417). 1:100 for flow cytometry analysis and 1:1000 for western blotting analysis.
For human samples: anti-HLA-DR-BV421 (307635; BioLegend; L243; B223586), anti-CD64-FITC (305005; BioLegend; 10.1; B216437), anti-CD86-FITC (374203; BioLegend; BU63; B274424), anti-CD14-PE (325605; BioLegend; HCD14; B188762), anti-CX3CR1-APC (341609; BioLegend; 2A9-1; B219658), anti-CD80-PerCP/Cy5.5 (305231; BioLegend; 2D10; B236173), anti-CD45-PE/Cy7 (304015; BioLegend; H130; B229088), anti-CD11c-PE/Cy7 (561356; BD Biosciences; B-ly6; 5114612), and Fc Receptor Blocking Solution (422301; BioLegend; B215860). 1:100 for all antibodies.

Validation

All the antibodies used were commercially available. The species and quality validation were performed by each manufacturer. Validation statements can be found on the following websites;

CD80-PB (104724; BioLegend)
https://www.biolegend.com/en-us/global-elements/pdf-popup/pacific-blue-anti-mouse-cd80-antibody-6267?filename=Pacific%20Blue%20anti-mouse%20CD80%20Antibody.pdf&pdfgen=true

anti-CD3-BV421 (100227; BioLegend)
https://www.biolegend.com/en-us/global-elements/pdf-popup/brilliant-violet-421-anti-mouse-cd3-antibody-7326?filename=Brilliant%20Violet%20421%20anti-mouse%20CD3%20Antibody.pdf&pdfgen=true

anti-Ly6G-BV421 (127627; BioLegend)
https://www.biolegend.com/en-us/global-elements/pdf-popup/brilliant-violet-421-anti-mouse-ly-6g-antibody-7161?filename=Brilliant%20Violet%20421%20anti-mouse%20Ly-6G%20Antibody.pdf&pdfgen=true

Streptavidin-BV421 (405226; BioLegend)
https://www.biolegend.com/en-us/global-elements/pdf-popup/brilliant-violet-421-streptavidin-7297?filename=Brilliant%20Violet%20421%20Streptavidin.pdf&pdfgen=true

anti-F4/80-BV421 (123137; BioLegend)
https://www.biolegend.com/en-us/global-elements/pdf-popup/brilliant-violet-421-anti-mouse-f4-80-antibody-7199?filename=Brilliant%20Violet%20421%20anti-mouse%20F480%20Antibody.pdf&pdfgen=true

CD86-PB (105021; BioLegend)
https://www.biolegend.com/en-us/global-elements/pdf-popup/pacific-blue-anti-mouse-cd86-antibody-3122?filename=Pacific%20Blue%20anti-mouse%20CD86%20Antibody.pdf&pdfgen=true

anti-I-A/I-E-Biotin (107603; BioLegend)
https://www.biolegend.com/fr-fr/global-elements/pdf-popup/biotin-anti-mouse-i-a-i-e-antibody-365?filename=Biotin%20anti-mouse%20I-AI-E%20Antibody.pdf&pdfgen=true

anti-CD11c-Biotin (117304; BioLegend)
https://www.biolegend.com/en-us/global-elements/pdf-popup/biotin-anti-mouse-cd11c-antibody-1814?filename=Biotin%20anti-mouse%20CD11c%20Antibody.pdf&pdfgen=true

anti-CD265 (RANK)-Biotin (13-6612-81; eBioscience)
https://www.thermofisher.com/order/genome-database/generatePdf?productName=CD265%20(RANK)&assayType=ANTIBODY&productId=13-6612-81&detailed=true

Lineage cell detection cocktail-Biotin (130-092-613; Miltenyi Biotec)
https://admin-shop-live.miltenyibiotec.com/DE-en/shop/comMiltenyiDatasheet/product?productId=16280

anti-CD3-PE (100308; BioLegend)
https://www.biolegend.com/en-us/global-elements/pdf-popup/pe-anti-mouse-cd3epsilon-antibody-25?filename=PE%20anti-mouse%20CD3epsilon%20Antibody.pdf&pdfgen=true

anti-CD140a-PE (135905; BioLegend)
https://www.biolegend.com/en-us/global-elements/pdf-popup/pe-anti-mouse-cd140a-antibody-6253?filename=PE%20anti-mouse%20CD140a%20Antibody.pdf&pdfgen=true

anti-CD45-FITC (103108; BioLegend)
https://www.biolegend.com/en-us/global-elements/pdf-popup/fitc-anti-mouse-cd45-antibody-99?filename=FITC%20anti-mouse%20CD45%20Antibody.pdf&pdfgen=true

anti-CX3CR1-FITC (149019; BioLegend)
https://www.biolegend.com/en-us/global-elements/pdf-popup/fitc-anti-mouse-cx3cr1-antibody-11878?filename=FITC%20anti-mouse%20CX3CR1%20Antibody.pdf&pdfgen=true

anti-Ly6C-APC (560595; BD Biosciences)
https://www.bdbiosciences.com/ds/pm/tds/560595.pdf

anti-CX3CR1-APC (149007; BioLegend)
https://www.biolegend.com/en-us/global-elements/pdf-popup/apc-anti-mouse-cx3cr1-antibody-10460?filename=APC%20anti-mouse%20CX3CR1%20Antibody.pdf&pdfgen=true

anti-CD45-PE/Cy7 (103114; BioLegend)
https://www.biolegend.com/en-us/global-elements/pdf-popup/pe-cy7-anti-mouse-cd45-antibody-1903?filename=PECy7%

20anti-mouse%20CD45%20Antibody.pdf&pdfgen=true

anti-CCR2-PE/Cy7 (150611; BioLegend)
https://www.biolegend.com/it-it/global-elements/pdf-popup/pe-cy7-anti-mouse-cd192-ccr2-antibody-13337?filename=PECy7%20anti-mouse%20CD192%20CCR2%20Antibody.pdf&pdfgen=true

anti-M-CSF (sc-365779; Santa Cruz Biotechnology; D4; B2417)
https://datasheets.scbt.com/sc-365779.pdf

anti-HLA-DR-BV421 (307635; BioLegend)
https://www.biolegend.com/en-us/global-elements/pdf-popup/brilliant-violet-421-anti-human-hla-dr-antibody-7226?filename=Brilliant%20Violet%20421%20anti-human%20HLA-DR%20Antibody.pdf&pdfgen=true

anti-CD64-FITC (305005; BioLegend)
https://www.biolegend.com/de-de/global-elements/pdf-popup/fitc-anti-human-cd64-antibody-536?filename=FITC%20anti-human%20CD64%20Antibody.pdf&pdfgen=true

anti-CD86-FITC (374203; BioLegend)
https://www.biolegend.com/it-it/global-elements/pdf-popup/fitc-anti-human-cd86-antibody-15111?filename=FITC%20anti-human%20CD86%20Antibody.pdf&pdfgen=true

anti-CD14-PE (325605; BioLegend)
https://www.biolegend.com/en-gb/global-elements/pdf-popup/pe-anti-human-cd14-antibody-3952?filename=PE%20anti-human%20CD14%20Antibody.pdf&pdfgen=true

anti-CX3CR1-APC (341609; BioLegend)
https://www.biolegend.com/nl-nl/global-elements/pdf-popup/apc-anti-human-cx3cr1-antibody-6605?filename=APC%20anti-human%20CX3CR1%20Antibody.pdf&pdfgen=true

anti-CD80-PerCP/Cy5.5 (305231; BioLegend)
https://www.biolegend.com/en-us/global-elements/pdf-popup/percp-cy5-5-anti-human-cd80-antibody-12382?filename=PerCPCy55%20anti-human%20CD80%20Antibody.pdf&pdfgen=true

anti-CD45-PE/Cy7 (304015; BioLegend)
https://www.biolegend.com/en-us/global-elements/pdf-popup/pe-cy7-anti-human-cd45-antibody-1915?filename=PECy7%20anti-human%20CD45%20Antibody.pdf&pdfgen=true

anti-CD11c-PE/Cy7 (561356; BD Biosciences)
https://www.bdbiosciences.com/ds/pm/tds/561356.pdf

Fc Receptor Blocking Solution (422301; BioLegend)
https://www.biolegend.com/en-us/global-elements/pdf-popup/human-trustain-fcx-fc-receptor-blocking-solution-6462?filename=Human%20TruStain%20FcX%20Fc%20Receptor%20Blocking%20Solution.pdf&pdfgen=true

Animals and other organisms

Policy information about studies involving animals; ARRIVE guidelines recommended for reporting animal research

Laboratory animals	-CX3CR1-EGFP knock-in mice and TRAP promoter-tdTomato transgenic mice derived on C57BL/6 (B6) background were backcrossed >10 generations onto DBA-1/J mice in our laboratory. -The FoxM1 LoxP/LoxP (fl/fl) mice were bred with Rosa26-CreERT2 mice by us. -Lyz2-Cre mice were provided by Dr. Akira (Osaka University). For most of the studies, 8-16 week old male mice were used.
Wild animals	The study did not involve wild animals.
Field-collected samples	The study did not involve samples collected from the field.
Ethics oversight	All mice were maintained in a specific pathogen-free animal facility in Osaka University. Up to five mice were housed per cage, which is changed every week and covered with nesting material for environmental enrichment. All animal experiments were performed in accordance with the Osaka University Animal Experimental Guidelines using approved protocols.

Note that full information on the approval of the study protocol must also be provided in the manuscript.

Human research participants

Policy information about studies involving human research participants

Population characteristics	The study involves blood, synovial fluid, and synovial samples from RA patients. All the subjects with RA fulfilled the ACR 2010 Rheumatoid Arthritis classification criteria. Details on age, gender, diagnosis, onset of disease, treatment, and seropositivity are given in Supplementary Table 2. 19 out of 23 patients were female. Average age was 69 years old. All the patients were under treatment of anti-rheumatic drugs. 17 out of 23 patients were seropositive.

Recruitment	Synovial tissue specimens were obtained from RA patients undergoing joint replacement surgery or synovectomy. Synovial fluid samples were obtained as excess material from RA patients with knee effusion undergoing therapeutic arthrocentesis. Because all the patients were under treatment of anti-rheumatic drugs or biological agents, it may have potential bias to the results. In addition, most of the patients who went joint replacement surgery had low disease activities in order to safely perform the surgery, which may also possess potential bias for the results.
Ethics oversight	Research involving human subjects was approved by the Institutional Review Board at Osaka University with appropriate informed consent.

Note that full information on the approval of the study protocol must also be provided in the manuscript.

Flow Cytometry

Plots

Confirm that:

☒ The axis labels state the marker and fluorochrome used (e.g. CD4-FITC).

☒ The axis scales are clearly visible. Include numbers along axes only for bottom left plot of group (a 'group' is an analysis of identical markers).

☒ All plots are contour plots with outliers or pseudocolor plots.

☒ A numerical value for number of cells or percentage (with statistics) is provided.

Methodology

Sample preparation	Described in the Methods sections.
Instrument	Described in the Methods sections.
Software	Described in the Methods sections.
Cell population abundance	After sorting CD45+CX3CR1+Ly6C+ cell populations, the sorted cells were passed through the cell sorter machine in order to determine the percentage of positive cells. The percentage of CD45+CX3CR1+Ly6C+cell populations was >95%.
Gating strategy	FACS strategies are provided in detail in the Supplementary Figure 8.

☒ Tick this box to confirm that a figure exemplifying the gating strategy is provided in the Supplementary Information.